

The effect of inertia and vertical confinement on the flow past a circular cylinder in a Hele-Shaw configuration

C.A. Klettner^{1,†} and F.T. Smith²

¹Department of Mechanical Engineering, University College London, Torrington Place, London WC1E 7JE, UK

²Department of Mathematics, University College London, 25 Gordon Street, London WC1H 0AY, UK

(Received 19 July 2021; revised 23 October 2021; accepted 9 December 2021)

The Poiseuille flow (centreline velocity U_c) of a fluid (kinematic viscosity ν) past a circular cylinder (radius R) in a Hele-Shaw cell (height $2h$) is traditionally characterised by a Stokes flow ($\Lambda = (U_c R/\nu)(h/R)^2 \ll 1$) through a thin gap ($\epsilon = h/R \ll 1$). In this work we use asymptotic methods and direct numerical simulations to explore the parameter space $\Lambda-\epsilon$ when these conditions are not met. Starting with the Navier–Stokes equations and increasing Λ (which corresponds to increasing inertial effects), four successive regimes are identified, namely the linear regime, nonlinear regimes I and II in the boundary layer (the ‘inner’ region) and a nonlinear regime III in both the inner and outer region. Flow phenomena are studied with extensive comparisons made between reduced calculations, direct numerical simulations and previous analytical work. For $\epsilon = 0.01$, the limiting condition for a steady flow as Λ is increased is the instability of the Poiseuille flow. However, for larger ϵ , this limit is at a much higher Λ , resulting in a laminar separation bubble, of size $O(h)$, forming for a certain range of ϵ at the back of the cylinder, where the azimuthal location was dependent on ϵ . As ϵ is increased to approximately 0.5, the secondary flow becomes increasingly confined adjacent to the sidewalls. The results of the analysis and numerical simulations are summarised in a plot of the parameter space $\Lambda-\epsilon$.

Key words: Hele-Shaw flows

1. Introduction

The study of Poiseuille flow through thin sheets past a circular cylinder has a long history, starting with the experiments by Hele-Shaw (1898) and the early theoretical work by Stokes (appendix to Hele-Shaw 1899). By neglecting inertial terms, the leading-order

† Email address for correspondence: ucemkle@ucl.ac.uk

solution was shown to be a quasi-two-dimensional potential flow past a cylinder, where all the boundary conditions are met except the no-slip boundary condition on the cylinder surface. The latter results in a boundary layer or ‘inner’ region of thickness $O(h)$ on the cylinder surface in which secondary flow becomes significant at leading order, whereas the secondary flow outside the boundary layer, in the ‘outer’ region, is only a higher-order effect; here h is the half-height of the gap. The fundamental interest in this problem has resulted in many different studies, which are reviewed below.

Riegels (1938) investigated experimentally and analytically the flow past a circular cylinder (radius R) in a Hele-Shaw configuration. The experiments showed a flow separation at approximately 60° from the rear stagnation point for $\Lambda = (U_c R/\nu)\epsilon^2 = 3$, where U_c is the maximum channel velocity and $\epsilon = h/R$. However, as the radius of the cylinder and the maximum channel velocity are not given in the work, reproduction of these results is difficult, as not only is the ratio h/R unknown but also the ratio R/W , where W is the width of the Hele-Shaw cell; blockage ratios can have a significant influence on Hele-Shaw flows (Thompson 1968). By retaining the inertial terms in the governing equations and seeking solutions in powers of Λ , an outer solution to $O(\Lambda)$ was obtained. Thompson (1968) used matched asymptotics to find inner and outer solutions, where both of these solutions were expanded in powers of h . Compared to the Riegels (1938) analysis, additional terms to the outer solution were determined, up to $O(\epsilon^2)$. The additional first-order term results in a displacement thickness of 0.6ϵ , indicating a degree of inner–outer regional interaction. The inner solutions, to $O(\epsilon)$, were resolved analytically (to give the tangential velocity) and using numerical calculations (for the radial and vertical velocities). In both of these works, the generation of higher-order streamwise vorticity was established, however, only in the outer flow solution.

Balsa (1998) investigated the boundary layer structure for a slender body with $h/l \ll 1$ (where l is a characteristic length of the slender body) using matched asymptotics, while retaining the inertial terms in the governing equations. Streamwise vorticity is diffused into the fluid domain and forms a pair of two counter-rotating corner vortices, the strength of which is dependent on the rate of change of the curvature of the body. This streamwise vorticity is confined to the boundary layer.

Lee & Fung (1969) used a construction technique to investigate the plane Poiseuille Stokes flow around a cylinder, which was found to be valid for $\epsilon < 5$. A two-term approximation to an infinite series was presented for the velocity and pressure fields, and from this a drag force could be derived, showing a dramatic decrease in drag for $\epsilon > 1$. Tsay & Weinbaum (1991) extended the work from Lee & Fung (1969), again using a construction technique to investigate the Stokes flow in a regular array of cylinders. The no-slip condition could be more accurately satisfied on the surfaces of the cylinders than in Lee & Fung (1969), thereby extending its range of validity in ϵ .

Guglielmini *et al.* (2011) and Sznitman *et al.* (2012) used particle image velocimetry and asymptotic methods to investigate the low-Reynolds-number (low- Re) flow past corners with varying radius of curvature. The secondary flow identified at the corner comprised pairs of counter-rotating vortices and was shown to be a purely viscous phenomenon. Owing to weak vertical velocities (in the z -direction, see figure 1) in a Hele-Shaw cell, depth-averaged solutions have also been investigated (Buckmaster 1970; Zhak, Nakoryakov & Safonov 1986). Zhak *et al.* (1986) also reported reversed flow for $\Lambda > 14$ in their laboratory experiments (where $\epsilon = 0.03$). The depth-averaged solutions did not predict the velocity field well near the cylinder.

There are many engineering applications that can be approximated as a plane Poiseuille flow through a thin sheet with cylinders of varying aspect ratio ϵ and cross-section

Flow past a cylinder in a Hele-Shaw configuration

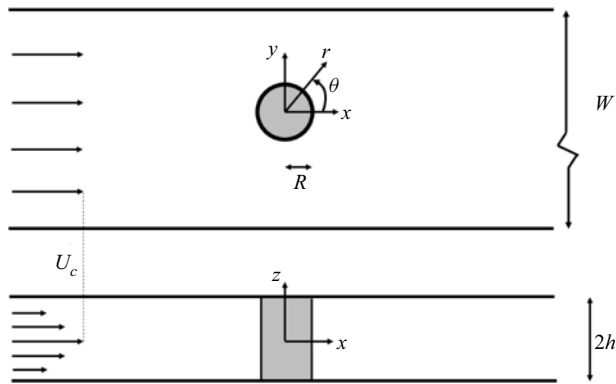


Figure 1. Schematic of Poiseuille flow (with maximum velocity U_c) past a cylinder (radius R), highlighted in grey, between two flat plates separated by a distance $2h$. The origin for the Cartesian and cylindrical polar coordinate system is the cylinder centre in the midplane. The span W is taken to be very large in this study.

aligned perpendicular to the flow, including flow through geological formations, which is important in the field of hydrology (Zimmerman & Bodvarsson 1996) and carbon sequestration (Fu 2016). In physiological flows, these types of flows are found in alveoli sacs (Lee 1969) and in the choriocapillaris (Zouache, Eames & Luthert 2015; Zouache *et al.* 2016). Knowledge of the flow past an isolated cylinder is fundamental to understanding mass and passive transfer in these critical tissues. The use of secondary flows has also microfluidic applications, including cell sorting (Nivedita, Ligrani & Papautsky 2017). Another example concerns microsystems handling off-chip and on-chip processes. An appreciation of the possible occurrence of considerable nonlinear effects, which might include flow separation and the formation of eddies, is felt to be potentially important; this is especially so if, as suggested here, such effects can arise at comparatively low flow rates (Kimura, Sakai & Fujii 2018).

The purpose of the present work is to study the development of the flow phenomena using asymptotic methods and direct numerical simulations, with the intention of increasing Λ and ϵ past the validity of Thompson's analysis. Starting with the Navier–Stokes equations (in cylindrical polar coordinates) and increasing Λ (which corresponds to increasing inertial effects), four successive regimes are identified, namely the linear regime, nonlinear regimes I and II in the boundary layer and a nonlinear regime III in both the inner and outer flow. Direct numerical simulations are carried out to investigate the parameter space where the analytical treatment is no longer valid. The governing equations and boundary conditions are defined in § 2, along with a description of the four regimes mentioned above. The numerical methods are described and validated in § 3, and the results for a variation in Λ and ϵ are presented in §§ 4 and 5, respectively. Discussion and conclusions are given in § 6.

2. Governing equations and boundary conditions

In this work we investigate a plane Poiseuille flow (with midplane velocity U_c) of a fluid (with a density and kinematic viscosity of ρ and ν , respectively) past a circular cylinder of radius R (see figure 1). The dimensional governing equations for a steady, incompressible, isothermal, Newtonian fluid are the continuity equation

$$\nabla \cdot \tilde{\mathbf{u}} = 0 \quad (2.1)$$

and the momentum equation

$$(\tilde{\mathbf{u}} \cdot \nabla)\tilde{\mathbf{u}} = -\frac{1}{\rho}\nabla\tilde{p} + \nu\nabla^2\tilde{\mathbf{u}}. \tag{2.2}$$

To non-dimensionalise this system, we set $\mathbf{u} = \tilde{\mathbf{u}}/U_c$, $\mathbf{x} = \tilde{\mathbf{x}}/R$ and $p = -2\tilde{p}/(GR) = \tilde{p}\Lambda/\rho U_c^2$, where $U_c = -Gh^2/(2\mu)$, μ is the dynamic viscosity, G is the far-field pressure gradient and h is half of the gap height. Here $\Lambda = (U_c R/\nu)(h/R)^2$. The non-dimensional equations are then

$$\nabla \cdot \mathbf{u} = 0 \tag{2.3}$$

and

$$\Lambda(\mathbf{u} \cdot \nabla)\mathbf{u} = -\nabla p + \epsilon^2\nabla^2\mathbf{u}, \tag{2.4}$$

where $\epsilon = h/R$. The boundary conditions include $p \sim -2x$ and $\mathbf{u} \rightarrow O(1)$ in the far field and no-slip conditions on $z = \pm\epsilon$ and at the cylinder surface. In cylindrical coordinates, (2.3) and (2.4) can be written as

$$\frac{1}{r}\frac{\partial(ru_r)}{\partial r} + \frac{1}{r}\frac{\partial u_\theta}{\partial \theta} + \frac{\partial u_z}{\partial z} = 0 \tag{2.5}$$

and

$$\left. \begin{aligned} \Lambda \left(u_r \frac{\partial u_r}{\partial r} + \frac{1}{r} u_\theta \frac{\partial u_r}{\partial \theta} + u_z \frac{\partial u_r}{\partial z} - \frac{1}{r} u_\theta^2 \right) &= -\frac{\partial p}{\partial r} + \epsilon^2 \left(\nabla^2 u_r - \frac{u_r}{r^2} - \frac{2}{r^2} \frac{\partial u_\theta}{\partial \theta} \right), \\ \Lambda \left(u_r \frac{\partial u_\theta}{\partial r} + \frac{1}{r} u_\theta \frac{\partial u_\theta}{\partial \theta} + u_z \frac{\partial u_\theta}{\partial z} + \frac{1}{r} u_r u_\theta \right) &= -\frac{1}{r} \frac{\partial p}{\partial \theta} + \epsilon^2 \left(\nabla^2 u_\theta - \frac{u_\theta}{r^2} + \frac{2}{r^2} \frac{\partial u_r}{\partial \theta} \right), \\ \Lambda \left(u_r \frac{\partial u_z}{\partial r} + \frac{1}{r} u_\theta \frac{\partial u_z}{\partial \theta} + u_z \frac{\partial u_z}{\partial z} \right) &= -\frac{\partial p}{\partial z} + \epsilon^2 \nabla^2 u_z, \end{aligned} \right\} \tag{2.6}$$

where the operator

$$\nabla^2(\cdot) = \frac{\partial^2(\cdot)}{\partial z^2} + \frac{1}{r}\frac{\partial}{\partial r}\left(r\frac{\partial(\cdot)}{\partial r}\right) + \frac{1}{r^2}\frac{\partial^2(\cdot)}{\partial \theta^2}$$

(Batchelor 1967).

Our interest lies in the flow behaviour for small values of ϵ and gradually increasing Λ , which corresponds to gradually increasing inertia and hence nonlinearity. Section 2.1 below addresses the linear regime. This is followed by nonlinear range I, which describes the first occurrence of significant nonlinearity in the flow field, given in § 2.2, after which § 2.3 is concerned with the next substantial change in nonlinear influence, which arises in the nonlinear range II. Section 2.4 is on the nonlinear range III, which represents the highest nonlinear regime.

2.1. Linear theory

We first take $\epsilon \ll 1$ (along with Λ being so small that all the inertia terms can be neglected) and work in two regions, each of which has $z = \epsilon z^*$. The outer region has all variables of

$O(1)$ except for $u_z = \epsilon u_z^*$ and $z = \epsilon z^*$, and so from (2.5) and (2.6) we obtain the lubrication equations

$$\frac{1}{r} \frac{\partial(ru_r)}{\partial r} + \frac{1}{r} \frac{\partial u_\theta}{\partial \theta} + \frac{\partial u_{z^*}}{\partial z^*} = 0, \tag{2.7a}$$

$$0 = -\frac{\partial p}{\partial r} + \frac{\partial^2 u_r}{\partial z^{*2}}, \tag{2.7b}$$

$$0 = -\frac{1}{r} \frac{\partial p}{\partial \theta} + \frac{\partial^2 u_\theta}{\partial z^{*2}}, \tag{2.7c}$$

$$0 = -\frac{\partial p}{\partial z^*}. \tag{2.7d}$$

Hence the pressure here depends only on r and θ to leading order. The appropriate boundary conditions require zero velocity components at $z^* = \pm 1$ and tangential flow at $r = 1$, along with the following at large r :

$$\left. \begin{aligned} \{u_\theta, u_r, u_{z^*}\} &\rightarrow \{-(1 - z^{*2}) \sin \theta, (1 - z^{*2}) \cos \theta, 0\}, \\ p &\sim -2x. \end{aligned} \right\} \tag{2.8}$$

At leading order, u_{z^*} is zero throughout the outer region, in keeping with the Hele-Shaw/Stokes (1899) finding that the dominant flow there is quasi-two-dimensional. The latter takes the form

$$\left. \begin{aligned} u_\theta &= -(1 - z^{*2}) \left(1 + \frac{1}{r^2}\right) \sin \theta, & u_r &= (1 - z^{*2}) \left(1 - \frac{1}{r^2}\right) \cos \theta, \\ p &= -2 \left(r + \frac{1}{r}\right) \cos \theta, \end{aligned} \right\} \tag{2.9a-c}$$

for the current circular cylinder geometry, and this leaves a non-zero slip velocity and associated pressure $p_0(\theta) = -4 \cos(\theta)$ as r tends to 1 on approach to the cylinder.

The inner region or boundary layer is where $r = 1 + \epsilon r^*$ and $z = \epsilon z^*$, with r^* and z^* of $O(1)$, $\theta = O(1)$ and $(u_\theta, u_r, u_z) = (\hat{u}_\theta, \epsilon \hat{u}_r, \epsilon \hat{u}_z) + \dots$, $p = p_0(\theta) + \epsilon^2 \hat{p}(r^*, \theta, z^*) + \dots$. From (2.5) and (2.6), we then find the equations

$$\text{at } O(1): \quad \frac{\partial \hat{u}_r}{\partial r^*} + \frac{\partial \hat{u}_\theta}{\partial \theta} + \frac{\partial \hat{u}_z}{\partial z^*} = 0, \tag{2.10a}$$

$$\text{at } O(\epsilon): \quad 0 = -\frac{\partial \hat{p}}{\partial r^*} + \nabla_1^2 \hat{u}_r, \tag{2.10b}$$

$$\text{at } O(1): \quad 0 = -p'_0(\theta) + \nabla_1^2 \hat{u}_\theta, \tag{2.10c}$$

$$\text{at } O(\epsilon): \quad 0 = -\frac{\partial \hat{p}}{\partial z^*} + \nabla_1^2 \hat{u}_z, \tag{2.10d}$$

where the ∇_1^2 operator is $(\partial^2/\partial r^{*2} + \partial^2/\partial z^{*2})$ and $p'_0 = \partial p_0/\partial \theta$. The boundary conditions in the inner region correspond to zero velocity components at $z^* = \pm 1$ and at $r^* = 0$, along

with the following matching requirement at large r^* :

$$\{\hat{u}_\theta, \hat{u}_r, \hat{u}_z\} \sim \{-2(1 - z^{*2}) \sin \theta, 2(r^* - b)(1 - z^{*2}) \cos \theta, 0\}, \tag{2.11a}$$

$$\hat{p}(r^*, \theta, z^*) \sim -2(r^* - b)^2 \cos \theta \tag{2.11b}$$

and (to emphasise) $p_0(\theta) = -4 \cos \theta$. The constant b represents an unknown origin shift and is to be addressed below. The θ -momentum balance (2.10c) combined with the boundary conditions on \hat{u}_θ determines \hat{u}_θ using

$$\nabla_1^2 \hat{u}_\theta = p'_0(\theta), \tag{2.12}$$

which in turn indicates an exponential decay into the outer \hat{u}_θ asymptote at large r^* . Equations (2.10a,b,d) then act to fix \hat{u}_r, \hat{u}_z and \hat{p} : for instance, they give the biharmonic-like equations

$$\left. \begin{aligned} \nabla_1^4 \hat{u}_r &= -\nabla_1^2 \left(\frac{\partial}{\partial \theta} \left(\frac{\partial u_\theta}{\partial r^*} \right) \right), \\ \nabla_1^4 \hat{u}_z &= -\nabla_1^2 \left(\frac{\partial}{\partial \theta} \left(\frac{\partial u_\theta}{\partial z^*} \right) \right), \end{aligned} \right\} \tag{2.13}$$

for \hat{u}_r and \hat{u}_z , noting that the right-hand sides of (2.13) are known by virtue of (2.12). We remark that the above working agrees with Thompson’s analysis.

2.2. Nonlinear range I

Now consider how substantial nonlinear influences emerge as Λ is increased slightly. Concerning the left-hand side of (2.10), the representative terms missed out are these:

$$\left. \begin{aligned} \Lambda \left(\hat{u}_r \frac{\partial \hat{u}_r}{\partial r^*} \epsilon + \hat{u}_\theta \frac{\partial \hat{u}_r}{\partial \theta} \epsilon + \hat{u}_z \frac{\partial \hat{u}_r}{\partial z^*} \epsilon - \hat{u}_\theta^2 \right) &\text{ versus } O(\epsilon), \\ \Lambda \left(\hat{u}_r \frac{\partial \hat{u}_\theta}{\partial r^*} \epsilon + \hat{u}_\theta \frac{\partial \hat{u}_\theta}{\partial \theta} \epsilon + \hat{u}_z \frac{\partial \hat{u}_r}{\partial z^*} \epsilon + \hat{u}_r \hat{u}_\theta \epsilon \right) &\text{ versus } O(1), \\ \Lambda \left(\hat{u}_r \frac{\partial \hat{u}_z}{\partial r^*} \epsilon + \hat{u}_\theta \frac{\partial \hat{u}_z}{\partial \theta} \epsilon + \hat{u}_z \frac{\partial \hat{u}_z}{\partial z^*} \epsilon \right) &\text{ versus } O(\epsilon). \end{aligned} \right\} \tag{2.14}$$

The terms after ‘versus’ correspond to the order present in (2.10). So, as Λ is increased, the first overtake (of the linear contributions) due to gradually increasing nonlinear effects occurs when the centrifugal (or centripetal) term $-\Lambda \hat{u}_\theta^2$ grows to be of order ϵ , as seen in (2.10b), as all other terms on the left-hand side are of smaller magnitude. This indicates that a new regime arises when

$$\Lambda = O(\epsilon), \tag{2.15}$$

a possibility that is examined below.

A similar study for the outer region shows that the missed-out terms there lag behind those of (2.7) by a factor Λ at most, and so they do not overtake significantly when (2.15) holds. When $\Lambda = O(\epsilon)$, with $\Lambda = \epsilon \Lambda'$, where Λ' is $O(1)$, then given that all terms on

the left-hand side of (2.14) are relatively small compared to the centripetal term, the new development is that (2.10*b*) is replaced by the augmented form

$$-\Lambda' \hat{u}_\theta^2 = -\frac{\partial \hat{p}}{\partial r^*} + \nabla_1^2 \hat{u}_r. \tag{2.16}$$

The other equations in the inner region, namely (2.10*a,c,d*), remain as they were and likewise for all the dominant equations (2.7) of the outer region.

We are now left with (2.10*a,c,d*) and (2.16) to solve. Here, however, (2.10*c*) still gives us (2.12) again for \hat{u}_θ , and so we are left with (2.10*a,d*) and (2.16). Eliminating the pressure now leads to

$$\nabla_1^4 \hat{u}_r = -\Lambda' \frac{\partial^2 \hat{u}_\theta^2}{\partial z^{*2}} - \nabla_1^2 \frac{\partial}{\partial \theta} \left(\frac{\partial \hat{u}_\theta}{\partial r^*} \right) \tag{2.17}$$

and

$$\nabla_1^4 \hat{u}_z = \Lambda' \frac{\partial^2 \hat{u}_\theta^2}{\partial z^* \partial r^*} - \nabla_1^2 \frac{\partial}{\partial \theta} \left(\frac{\partial \hat{u}_\theta}{\partial z^*} \right), \tag{2.18}$$

as the two equations for \hat{u}_r and \hat{u}_z , respectively. The boundary conditions require zero velocities at $r^* = 0$ and at $z^* = \pm 1$, along with the following at large r^* :

$$\left. \begin{aligned} \{\hat{u}_\theta, \hat{u}_r, \hat{u}_z\} &\sim \{-2(1 - z^{*2}) \sin \theta, 2(r^* - b)(1 - z^{*2}) \cos \theta + \Lambda' \hat{u}_1(\theta, z^*), 0\}, \\ \hat{p}(r^*, \theta, z^*) &\sim -2(r^* - b)^2 \cos \theta + \frac{96}{35} \Lambda' r^* \sin^2 \theta, \end{aligned} \right\} \tag{2.19}$$

cf. (2.11*a,b*), where

$$\hat{u}_1(\theta, z^*) = -4 \left[z^{*2} \left(\frac{11}{70} - \frac{z^{*2}}{6} + \frac{z^{*4}}{30} \right) - \frac{1}{42} \right] \sin^2 \theta. \tag{2.20}$$

The required behaviours (2.19) are to match the velocity components and pressure with those of the outer region as r tends to unity. The form (2.20) of the (new) term proportional to Λ' in (2.19) is inferred directly from the governing equations in the inner region. The three turning points or extrema present in the radial velocity (u_r) condition at large r^* originate from the requirement (see (2.20)) that the vertical velocity (u_z) must tend to zero in order to match with the solution in the outer region. In consequence, the total effective mass flux, the integral of u_r with respect to z^* across the channel, must be zero from the continuity equation in (2.23); this, combined with the velocity u_r itself having to be zero at the walls and given the symmetry about $z^* = 0$, necessitates at least three extrema being encountered. It should be noted that Riegels' (1938) analysis also assumed that $\int_{-h}^h u_r dz = 0$, while Thompson's (1968) matched asymptotic approach did not require this condition and showed that this condition is not valid, except as $\epsilon \rightarrow 0$.

2.3. Nonlinear range II

The next distinct nonlinear range arises because of the presence of the contribution in Λ' in the radial velocity in (2.19). In the inner region, when Λ' becomes large with r^* remaining of the order of unity, the centrifugal term, which is of order ϵ in (2.14), increases like Λ' whereas the inertial contribution $\Lambda u_r \partial u_r / \partial r$ (see (2.6)) grows as $\Lambda \epsilon \Lambda'^2$ in view of the $O(1)$ form of \hat{u}_1 in (2.19). A new balance between that inertial contribution and the

centrifugal effect therefore takes place when $\Lambda \epsilon \Lambda^{1/2}$ grows to become comparable with $\epsilon \Lambda'$. This balance implies that the new regime is defined by

$$\Lambda = O(\epsilon^{1/2}). \tag{2.21}$$

Essentially the same overtaking occurs for the other inertial contributions. Hence, following on from the previous range, the second nonlinear range therefore has Λ increased to $\Lambda = \epsilon^{1/2} \Lambda''$ with Λ'' of $O(1)$ and in the inner region the new expansion is

$$\left. \begin{aligned} (u_\theta, u_r, u_z) &= (\bar{u}_\theta, \epsilon^{1/2} \bar{u}_r, \epsilon^{1/2} \bar{u}_z) + \dots, \\ p &= \bar{p} + \epsilon^{3/2} \bar{\bar{p}}(\theta, r^*, z^*) + \dots \end{aligned} \right\} \tag{2.22}$$

Here, $\bar{p} = p_0(\theta)$ from matching. Substitution into (2.5) and (2.6) yields to leading order the following system:

$$\left. \begin{aligned} O(\epsilon^{-1/2}): \quad & \frac{\partial \bar{u}_r}{\partial r^*} + \frac{\partial \bar{u}_z}{\partial z^*} = 0, \\ O(\epsilon^{-1/2}): \quad & \Lambda'' \left(\bar{u}_r \frac{\partial \bar{u}_r}{\partial r^*} + \bar{u}_z \frac{\partial \bar{u}_r}{\partial z^*} - \bar{u}_\theta^2 \right) = -\frac{\partial \bar{\bar{p}}}{\partial r^*} + \left(\frac{\partial^2 \bar{u}_r}{\partial r^{*2}} + \frac{\partial^2 \bar{u}_r}{\partial z^{*2}} \right), \\ O(1): \quad & \Lambda'' \left(\bar{u}_r \frac{\partial \bar{u}_\theta}{\partial r^*} + \bar{u}_z \frac{\partial \bar{u}_\theta}{\partial z^*} \right) = -p'_0(\theta) + \left(\frac{\partial^2 \bar{u}_\theta}{\partial r^{*2}} + \frac{\partial^2 \bar{u}_\theta}{\partial z^{*2}} \right), \\ O(\epsilon^{-1/2}): \quad & \Lambda'' \left(\bar{u}_r \frac{\partial \bar{u}_z}{\partial r^*} + \bar{u}_z \frac{\partial \bar{u}_z}{\partial z^*} \right) = -\frac{\partial \bar{\bar{p}}}{\partial z^*} + \left(\frac{\partial^2 \bar{u}_z}{\partial r^{*2}} + \frac{\partial^2 \bar{u}_z}{\partial z^{*2}} \right). \end{aligned} \right\} \tag{2.23}$$

Here we observe that $\Lambda'' = (U_c R/\nu)\epsilon^{3/2}$; this is equivalent to a Dean number. The boundary conditions for (2.23) are that the three velocity components are zero at $z^* = \pm 1$ and at $r^* = 0$, along with the following at large r^* :

$$\left. \begin{aligned} \{\bar{u}_\theta, \bar{u}_r, \bar{u}_z\} &\sim \{-2(1 - z^{*2}) \sin \theta, \Lambda'' \hat{u}_1(\theta, z^*), 0\}, \\ \frac{\partial \bar{\bar{p}}}{\partial r^*} &\rightarrow \frac{96}{35} \Lambda'' \sin^2 \theta, \end{aligned} \right\} \tag{2.24}$$

where \hat{u}_1 is defined in (2.20). The boundary condition for the pressure in (2.24) applies because the order of magnitude of the pressure in (2.22) arises in response to the inertial and viscous forces in the inner region rather than in response to the outer flow pressure.

2.4. Nonlinear range III

The previous two subsections indicate that nonlinear effects arise first in the boundary layer, involving the two regimes associated with (2.15) and (2.21). The next nonlinear range III would seem to correspond, tentatively, to considerable nonlinear influences first entering the outer flow and to have a regime scale of $\Lambda = O(1)$. The reasoning for the $O(1)$ scale here is based on the pressure gradient in (2.24) in particular, since it implies a pressure contribution of order $\epsilon^{3/2} \Lambda'' r^*$ near the edge of the boundary layer. As the outer flow is entered (where r^* increases to the order ϵ^{-1}), this pressure contribution grows to become of order unity when Λ'' increases by $\epsilon^{-1/2}$, i.e. when Λ becomes $O(1)$, at which stage the outer flow is affected nonlinearly. This inference is to be appraised further after the study of direct numerical solutions and reduced system solutions to be presented in the following sections.

3. Numerical methods

In the previous section, systems of equations of increasing complexity were derived, which require a numerical solution. In this section, we detail the methods used, mostly for the Navier–Stokes system (2.1) and (2.2) and their validation.

3.1. Navier–Stokes simulations

Numerical simulations of (2.1) and (2.2) were carried out with the open-source computational fluid dynamics toolbox OpenFOAM using a finite-volume method (Weller *et al.* 1998). Three-dimensional unstructured meshes were generated in *blockMesh* and the solver used was *simpleFoam*, which is appropriate for these laminar steady flows. All schemes are second-order-accurate. The cylinder is placed in the middle of a domain of length $L = 200R$ and width $W = 100R$, such that the flow at the sides is not affected by the cylinder (a schematic of the set-up is shown in figure 1). The cylinder and the top and bottom plates have the no-slip condition applied, while the sidewalls have the no-flux condition. The inlet condition is that of Poiseuille flow (with the flow from left to right) and the outlet condition is $p = 0$. The validation and mesh independence studies are shown in the next section and in Appendix A, respectively.

3.1.1. Validation

The purpose of this validation is to ensure OpenFOAM's ability to accurately simulate flow past vertically confined cylinders. The most recent comprehensive comparison of experiments and numerical simulations for flow past confined cylinders with varying aspect ratio is by Ribeiro *et al.* (2012). Although the blockage ratio (R/W) of 25 % is much higher than for the current work, the salient phenomena of the flow around a confined cylinder are present, such as flow separation with increasing Reynolds number and the variation of the separation bubble in the vertical direction, which gives confidence to the numerical solutions for the unbounded set-up considered in this work. The geometry used was for an aspect ratio, $h/R = 2$. Following Ribeiro *et al.* (2012) the cylinder is placed in the centre of the channel (width $4R$) $200R$ and $140R$ from the inlet and outlet, respectively (to minimise the effects of the inlet and outlet). All boundaries had the no-slip condition except for the inlet and the outlet. The definition of the Reynolds number for this problem was $Re = QR/(Av)$, where Q and A are the volume flow rate and cross-sectional area, respectively, and $U = Q/A$ is the bulk velocity. Comparisons were made across a wide range of Reynolds numbers for the separation bubble length L_v (defined as the distance from the rear stagnation point on the cylinder to the location in the wake where the streamwise velocity is zero) and velocity profiles fore and aft of the cylinder, with good agreement found in all cases (see figures 2 and 3).

The comparison with the analytical work by Thompson (1968) forms the second part of the validation, which is for unbounded flow past a circular cylinder in a Hele-Shaw configuration. Extensive comparisons between the current numerical work and Thompson's analytical solution for a wide range of Λ are given in § 4, and are not repeated here. Also, as the comparison to Thompson's (1968) paper forms a significant part of this work, the inner and outer solutions for the radial and tangential velocity and pressure have been included in Appendix B. Thompson's outer solution (for velocity and pressure) is given up to $\Lambda = O(\epsilon^2)$, while the inner solution is up to $\Lambda = O(\epsilon)$, which needs to be considered when comparisons are made with the present direct numerical simulations.

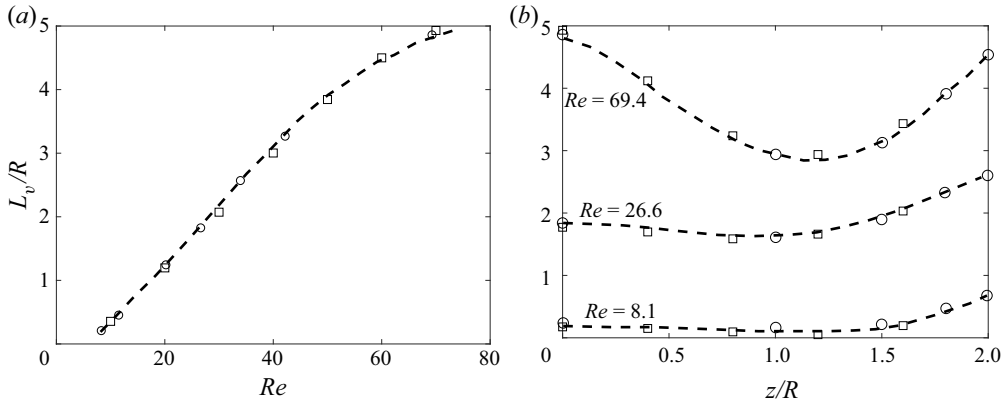


Figure 2. Variation of the length of the laminar separation bubble L_v with (a) Reynolds number and (b) vertical distance with the current simulations (squares) and numerical simulations and experiments by Ribeiro *et al.* (2012) given by the dashed black lines and circles, respectively.

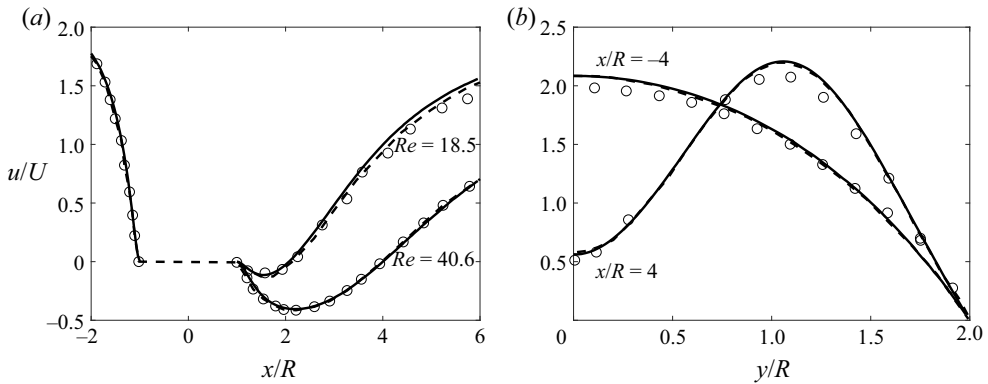


Figure 3. Streamwise velocity variation in the (a) streamwise direction at $z/R = 0$ and $y/R = 0$ for $Re = 18.5$ and $Re = 40.6$ and (b) cross-stream direction at $z/R = 0$ and $x/R = \pm 4$ for $Re = 26.1$. Shown are the current simulations (black lines) and the numerical simulations (dashed black lines) and experiments (circles) by Ribeiro *et al.* (2012).

3.2. Reduced system calculations

The reduced system descriptions are those of §§ 2.1–2.3. For the linear theory case of § 2.1, the outer flow is given by (2.11) and the inner flow by (2.12) and (2.13). These were treated by a standard relaxation method based on finite differences to determine the three scaled velocity components, which has been used in previous studies (Glowinski & Pironneau 1979; Smith & Dennis 1990). The formulation here is a velocity–vorticity one, supplemented by iterative determination of the constant b through an integral of the continuity equation over the inner-region domain. Agreement was found with the results of Thompson (1968) including the value 0.6302 of the constant b . The same finite-difference method was then extended to cover nonlinear range I for the system (2.17)–(2.18).

The system of equations in nonlinear range II (2.23) can be independently calculated in the z^*-r^* plane for different azimuthal locations. The question arises as to the length of the domain in the radial direction, as the boundary condition (2.24) is independent

of r^* . One possibility is matching the asymptotic boundary condition for u_r to the numerical simulation data, which is further explored in § 4.5.

4. Results: variation of Λ

In this section, the results of the numerical simulations will be presented, and where appropriate compared to previous analytical work, for $\epsilon = 0.01$ and increasing Λ . These values have been chosen to highlight the different ranges identified in § 2. First, the velocity fields of the linear range will be presented, which also serves as further validation of the numerical methods. Next, as the nonlinear ranges identified in § 2 do not have explicitly defined limits, distinct flow phenomena cannot be allocated neatly to separate ranges. Therefore, flow and force diagnostics will be presented for increasing Λ , and the overall discussion is left to § 6.

4.1. Linear range

To investigate the linear range, simulations of $\Lambda = 0.001$ were carried out, such that $\Lambda \ll \epsilon \ll 1$. Figure 4 shows the comparison of the three velocity components between the current direct numerical simulations, reduced calculations and Thompson's analytical work at different azimuthal locations (which is measured from the rear stagnation point). In the outer region there is excellent agreement for the tangential, radial and vertical velocities between the current numerical simulations, Thompson's outer solution and the linear theory. In the inner region there is excellent agreement between the direct numerical simulations, reduced calculations and Thompson's inner solution. Note how the inner and outer solutions provide an agreeable composite solution to the numerical simulation results. The constant displacement thickness of approximately 0.6ϵ can be identified as the vertical shift between the linear solution given by (2.9a–c) and the present simulations or Thompson's outer solution (see figure 4d); our calculation of b in the linear range in § 2.1 is based on a solvability requirement that is equivalent to Thompson's approach and involves the total mass flux, and the result for b agrees well with the numerical simulation results. The boundary layer thickness is approximately $r^* = 2$, which was predicted in the early work by Stokes. The vertical velocity is orders of magnitude less than the radial and tangential velocities and is only present in the inner layer. The velocity profiles exhibit a symmetry around $\theta = \pi/2$ for $\Lambda = 0.001$, however as Λ is increased the vertical and radial velocity become increasingly asymmetric.

4.2. Streamlines perpendicular to cylinder surface

To gain a qualitative picture of the secondary flow induced by increasing Λ , streamline plots of u_z and u_r (obtained from the direct numerical simulations) in planes perpendicular to the cylinder surface ($z^* - r^*$), at different angles from the rear stagnation point, are shown in figure 5. In nonlinear range I, the important addition to the governing equations is the centrifugal term in (2.16), which occurs when Λ is $O(\epsilon)$. For $\Lambda = 0.05$, there is an upwelling in the component u_r in the midplane (at $z^* = 0$) at $\theta \approx \pi/2$ (see figure 5b,c), which is a consequence of the centrifugal term (i.e. inertia) and occurs at the midplane because the centrifugal force is greatest there. For increasing Λ , the start of the upwelling moves closer to the front stagnation point, which is then followed by the streamlines wrapping around themselves, forming two counter-rotating vortices. Also, for the same angle from the rear stagnation point, these counter-rotating vortices increase in size for increasing Λ (e.g. figure 5c,h,m for 92°). In figure 5, attention needs to be taken when

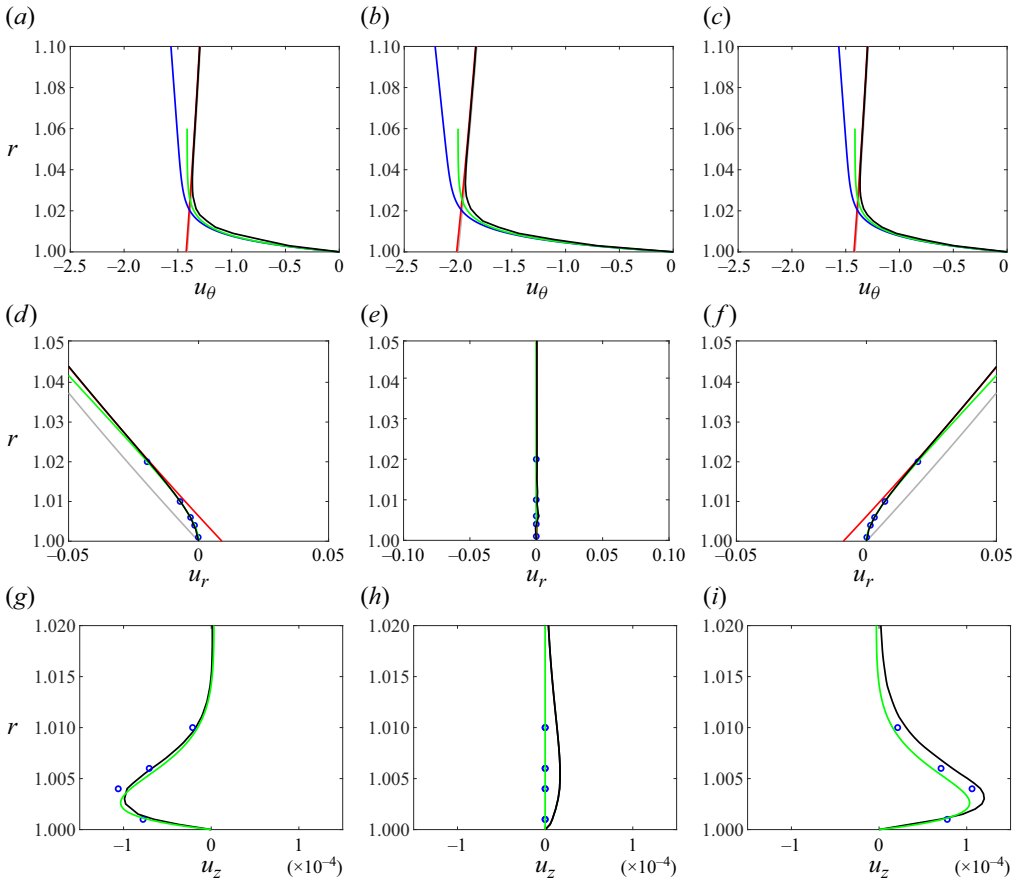


Figure 4. The (a–c) tangential, (d–f) radial and (g–i) vertical velocity profiles at (a, d, g) $\theta = 3\pi/4$, (b, e, h) $\theta = \pi/2$ and (c, f, i) $\theta = \pi/4$ for $\epsilon = 0.01$ and $\Lambda = 0.001$. The lines represent the present Navier–Stokes numerical simulations (black lines), present reduced calculations for the inner region (2.12)–(2.13) (green lines), Thompson’s inner solution (blue lines and circles), Thompson’s outer solution (red line) and the linear outer solution (2.11) (grey line). The profiles are in the midplane ($z = 0$) for (a–f) and at $z^* = -0.4$ for (g–i).

considering the scale of the counter-rotating vortices. For example, for $\Lambda = 1$, the two counter-rotating vortices grow to about $r^* = 60$ (or $0.6R$) and as $\epsilon = 0.01$, these are highly elongated flow structures (figure 5m).

To compare the streamline structure of the direct numerical simulations against Thompson’s (1968) outer solution (red lines) and the current reduced calculations for nonlinear range I (2.16)–(2.18) (green lines), the locations of where $u_r = 0$ are shown in figure 5. Note that, in figure 5, for Thompson’s work $u_r < 0$ (i.e. the flow is towards the cylinder) and $u_r > 0$ (i.e. the flow is away from the cylinder) for radial locations further away and closer to the cylinder than the red line, respectively. Thompson’s work consistently underpredicts the results of the numerical simulations, while the comparison with the reduced calculations is good for azimuthal locations away from $\pi/2$ and for low Λ . Metrics of the counter-rotating vortices are analysed in more detail in the next section. When $\theta < \pi/2$, the pressure gradient and the centrifugal terms are coincident and the domed structure of where $u_r = 0$ seen for $\theta > \pi/2$ is not present. The counter-rotating

Flow past a cylinder in a Hele-Shaw configuration

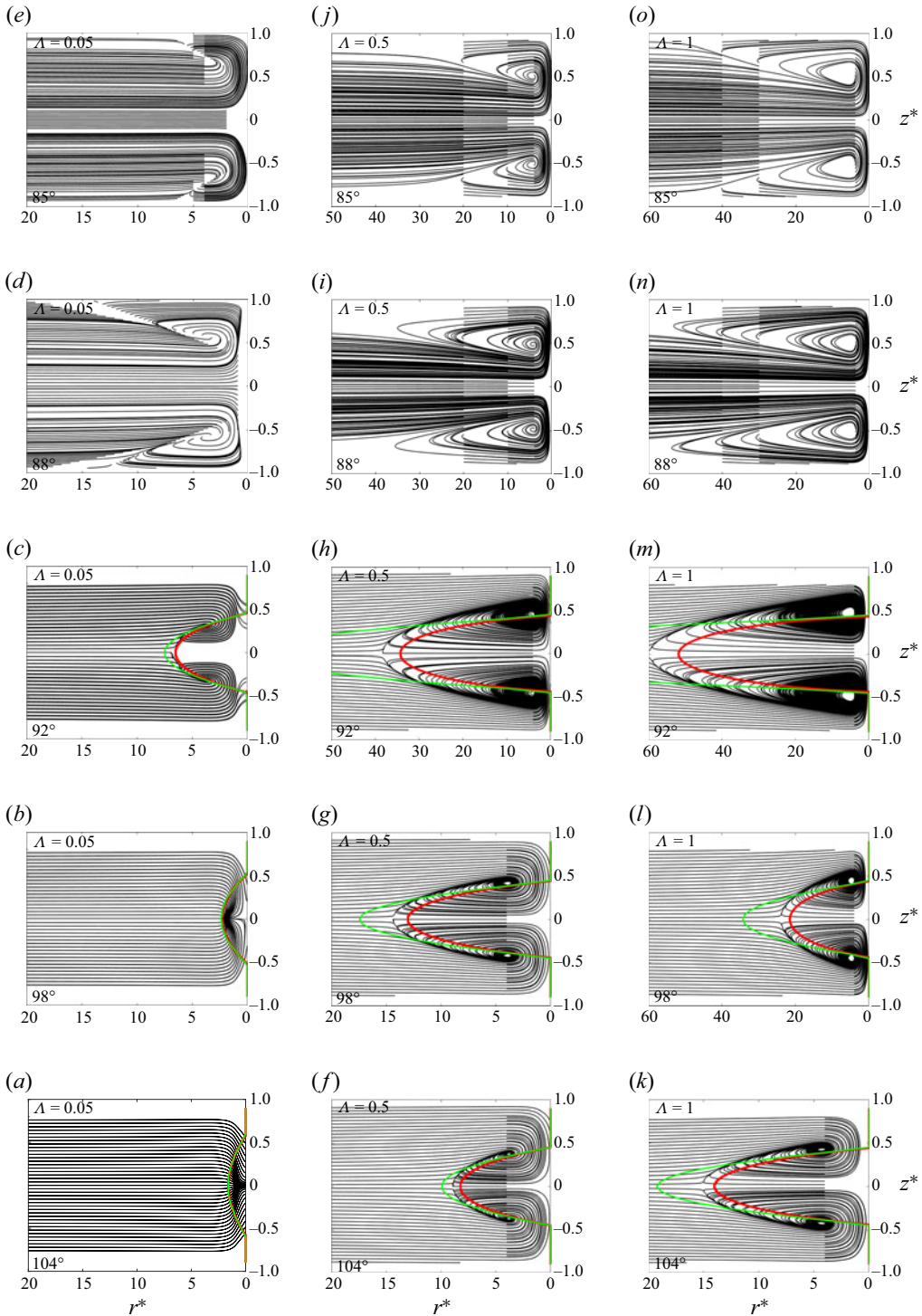


Figure 5. Streamlines of u_z and u_r in planes normal to the cylinder surface (z^*-r^*) for (a–e) $\Lambda = 0.05$, (f–j) $\Lambda = 0.5$ and (k–o) $\Lambda = 1$. All results are for $\epsilon = 0.01$. The angle of the plane (from the rear stagnation point) is shown in the left corner. The red and green lines indicate the locations of where $u_r = 0$ for Thompson’s outer solution and the reduced calculations for nonlinear range I (2.13) and (2.16), respectively. Note the scale for r^* ; for $\Lambda = 1$, these are highly elongated vortices close to $\theta = \pi/2$.

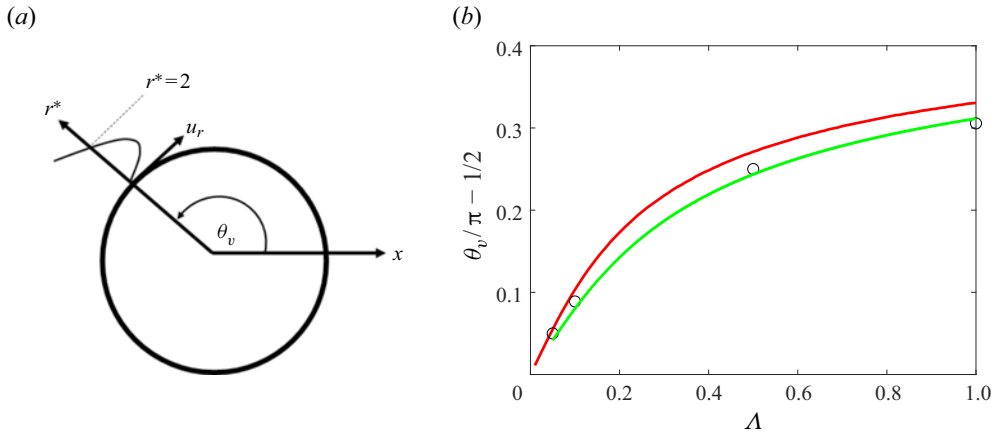


Figure 6. (a) Definition of the angle θ_v (where the flow is from left to right) and (b) its variation with Λ (for $\epsilon = 0.01$), where the present simulations are shown (circles), along with Thompson’s theoretical value (red line) and the reduced calculations for nonlinear range I (green line).

vortices becoming smaller (for decreasing azimuthal location) and the flow towards the cylinder is increasingly confined to the channel walls (for θ tending towards zero).

4.3. Pair of counter-rotating vortices

The two metrics of interest here are the angle θ_v at which the pair of counter-rotating vortices start to form (where the angle is measured from the rear stagnation point) and the size L_v of the two counter-rotating vortices. Firstly, θ_v is defined to be the largest angle from the rear stagnation point, where $u_r = 0$ along the radial coordinate, but that it is at least $r^* = 2$ (see figure 6a). This definition is used to overcome the issue of Thompson’s outer solution for u_r not satisfying the no-slip condition on the cylinder surface (see the red line in figure 4d), so the outer solution for u_r would predict the presence of streamwise vorticity, even in the linear regime. Figure 6(b) shows that, as Λ is increased, the upwelling due to u_r moves closer to the front stagnation point. The excellent agreement with the reduced calculations in figure 6(b) implies that the centrifugal term alone determines the starting point of the upwelling of u_r for this range of Λ . Secondly, the size of the counter-rotating vortices is defined to be the distance from the cylinder surface in the midplane ($z = 0$) to where $u_r = 0$ (see inset in figure 7a). For the reduced calculations, L_v was found to be proportional to Λ . From the direct numerical simulations in figure 7(a,b), it can be seen that the growth of the counter-rotating vortices is not proportional to Λ due to the additional nonlinear terms in (2.14) being important when Λ is $O(1)$ and then only near $\theta = \pi/2$.

Thompson’s (1968) results in figures 6 and 7 are applicable up to $\Lambda = O(1)$, while Thompson’s inner solution (up to $O(\epsilon)$) for u_r is symmetric about $\theta/\pi = 1/2$ and has no change of sign in the radial direction r^* (and therefore cannot be used to predict θ_v). In contrast, the reduced calculations in the current work are an inner solution. This might explain why Thompson’s analysis is better at predicting L_v , while the present reduced calculations are better at predicting θ_v . Although our interest here is to a large extent in the flow structure as Λ increases, we should comment that in figure 7 the nonlinear range I results (in green) are almost certainly taken beyond their practical range of application.

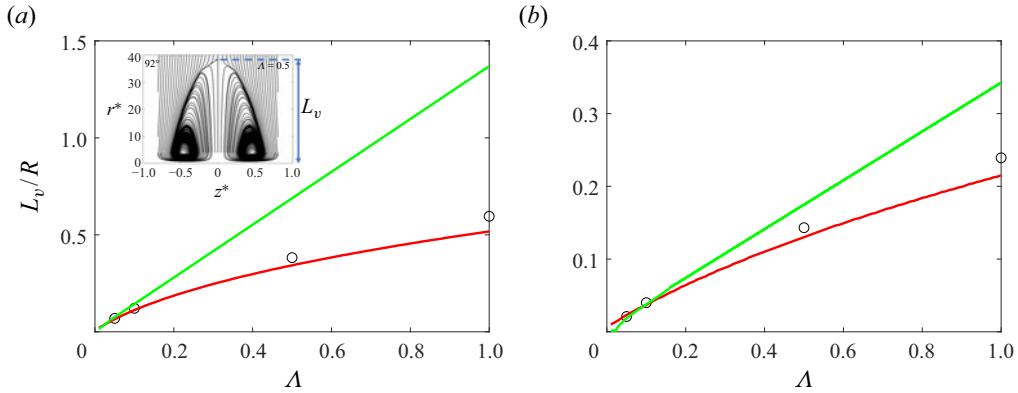


Figure 7. Variation of the size of the counter-rotating vortices, L_v/R , in the midplane at (a) 92° and (b) 98° with Λ (for $\epsilon = 0.01$), where the present simulations are shown (circles), along with Thompson's theoretical value (red line) and the reduced calculations for nonlinear range I (green line).

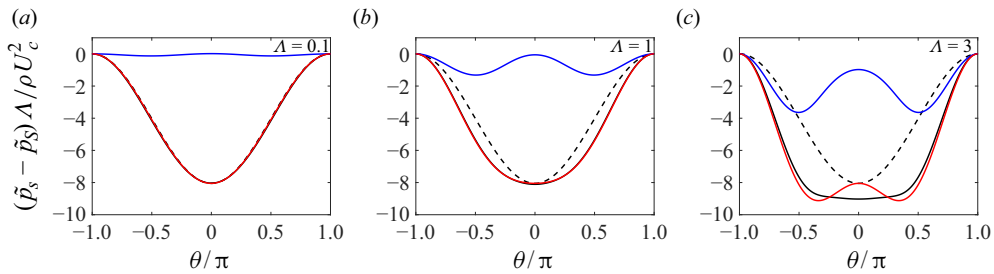


Figure 8. The variation of the midplane ($z = 0$) surface pressure coefficient $(\tilde{p}_s - \bar{p}_s)\Lambda/\rho U_c^2$ (where \tilde{p}_s is the pressure at $\theta = \pi$) with azimuthal location for the current direct numerical simulations (black line), the linear solution (black dashed lines) and Thompson's (1968) solution (red lines) for $\Lambda = 0.1$ (a), 1 (b) and 3 (c). The blue line gives the pressure perturbation of the direct numerical simulations from the linear solution.

4.4. Pressure field

In figure 8(a–c) the midplane surface pressure coefficient, $(\tilde{p}_s - \bar{p}_s)\Lambda/\rho U_c^2$, where \tilde{p}_s and \bar{p}_s are the surface pressure and the pressure at the front stagnation point, respectively, is plotted for increasing Λ . For small Λ , the linear solution (2.9a–c) and Thompson's pressure solution (B4) agree with the current direct numerical simulations. For $\Lambda = 1$, the agreement of the current simulations and Thompson's solution remains close while deviating from the Stokes solution. For $\Lambda = 3$, Thompson's solution agrees with the simulations on the front side of the cylinder; however, it does not predict the behaviour on the rear side of the cylinder, significantly underestimating the drop in pressure there. Also plotted is the pressure perturbation of the direct numerical simulations from the linear solution (blue line), which is found to scale in proportion to $\Lambda \sin^2 \theta$ and is consistent with the asymptotic analysis and Thompson's analysis (see boundary condition (2.19) and Thompson's solution (B4), respectively).

In nonlinear range I, it is possible to calculate the gradients of the pressure perturbations (from the linear pressure solution) in the radial and the vertical directions. These pressure gradients, for example at the walls, were obtained from numerical derivatives of the vorticity functions that were used in the nonlinear range I calculations (see (C4) and (C5) in Appendix C). In figure 9(a) the inner solution of the present reduced calculations

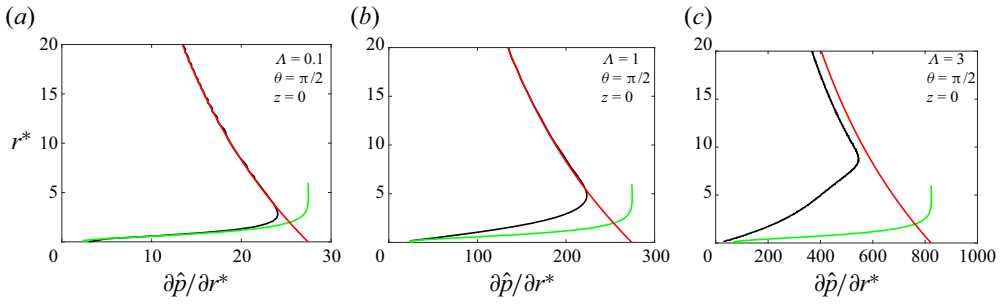


Figure 9. Profiles of the radial gradient of the pressure perturbation for $\Lambda = 0.1$ (a), 1 (b) and 3 (c) for the current direct simulations (black lines), Thompson's outer solution (red lines) and nonlinear range I (green lines).

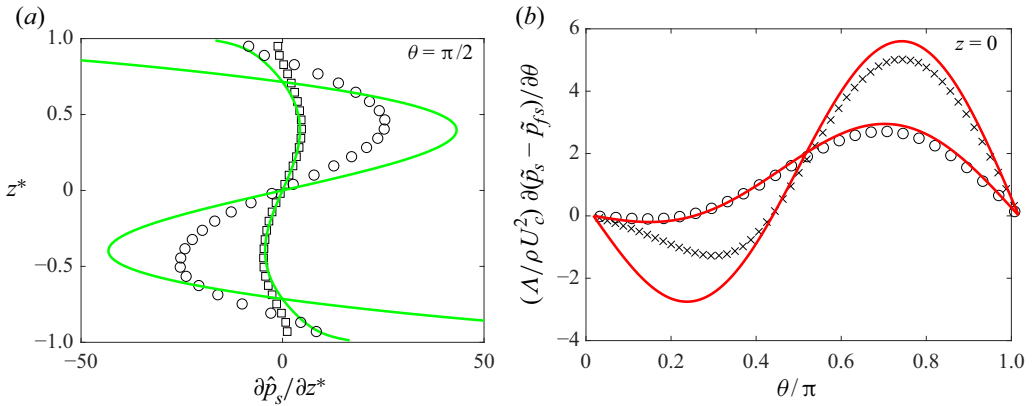


Figure 10. Profiles of the gradient of the (a) surface pressure perturbation in the vertical direction and (b) surface pressure minus the free-stream pressure \tilde{p}_{fs} in the azimuthal direction for the current direct simulations for $\Lambda = 0.1$ (\square), 1 (\circ) and 3 (\times). Thompson's outer solution (red lines) and nonlinear range I (green lines) are also shown. The free-stream pressure, $\tilde{p}_{fs}(x)$, is the pressure in the channel far away from the cylinder (at the same streamwise location) projected onto the cylinder.

and Thompson's outer solution provide, in effect, an agreeable composite solution to the direct numerical simulations for the radial gradient of the pressure perturbation for $\Lambda = 0.1$. As Λ is increased, the direct numerical simulations and the inner solution start to diverge, which is to be anticipated, as $\Lambda = 1$ is beyond the range of applicability of nonlinear range I. Similarly, the numerical simulations start to diverge from Thompson's outer solution when Λ is further increased to $\Lambda = 3$. The vertical gradient of the surface pressure perturbation is plotted in figure 10(a). As could be anticipated, the variation is weak, and as Λ is increased, the agreement between the nonlinear range I and the direct numerical simulations decreases. Note that Thompson does not calculate an inner pressure solution, so it is not possible to make comparisons with the current numerical simulations in this region.

As the fluid flows through the channel and past the cylinder, there are two main pressure gradients, namely, the pressure gradient in the channel from the inlet to the outlet and also the pressure gradient due to the presence of the cylinder. When Λ is sufficiently small, the channel pressure gradient is dominant. However, as Λ is increased, the channel pressure

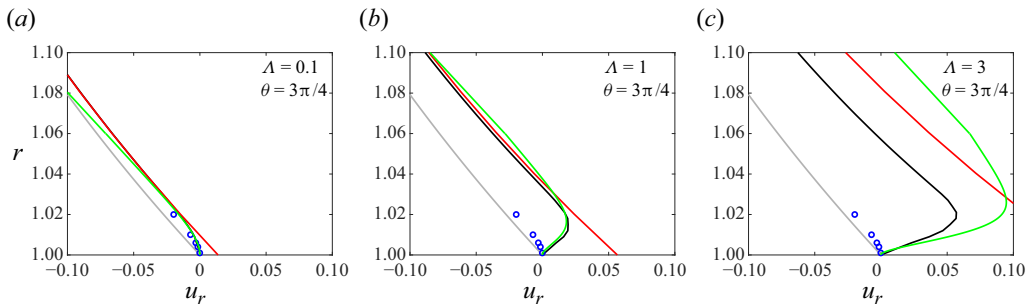


Figure 11. The radial velocity profiles at $\theta = 3\pi/4$ (in the midplane, $z = 0$) for $\Lambda = 0.1$ (a), 1 (b) and 3 (c). The lines represent the current Navier–Stokes numerical simulations (black line), Thompson’s inner solution (blue circles), Thompson’s outer solution (red line), the potential flow solution (grey line) and the reduced calculations for nonlinear range I (green line).

gradient is decreased, resulting in the cylinder pressure gradient having an increased effect on the flow. To highlight this, in figure 10(b), the free-stream pressure $p_{fs}(x)$ (i.e. far enough away for the cylinder to have no effect) is subtracted from the pressure at the surface of the cylinder. As expected, on the front of the cylinder there is a favourable pressure gradient (with reasonable agreement with Thompson’s outer solution), but as Λ is further increased, an adverse pressure gradient emerges at the rear of the cylinder at $\theta/\pi \approx 0.4$ for $\Lambda = 3$, which results in a deceleration in the tangential velocity at the back of the cylinder (see later figure 14f).

4.5. Velocity field

In this section the velocity field will be discussed for increasing Λ . As the tangential velocity u_θ remains largely unchanged until Λ is $O(1)$, we start with a detailed examination of u_r , which is instrumental in the formation of the counter-rotating vortices and is key to the reduced calculations in nonlinear range II, and then we progress to the tangential velocity. As u_z is weak for the range of Λ considered, it will not be discussed here.

To highlight how the secondary flow structure relates to the radial velocity, midplane velocity profiles of u_r are plotted in figure 11 for different Λ at $\theta = 3\pi/4$. There is good agreement between the direct numerical simulations and the reduced calculations of this work for nonlinear range I (2.16)–(2.18) (see Appendix C for further details on how u_r is calculated in nonlinear range I) and Thompson’s outer and inner solutions where they are applicable, while for $\Lambda = 3$, as is to be anticipated, there are significant differences. Note that $u_r = 0$ was used to indicate the domed structure seen in figure 5.

As Λ is increased from the linear to nonlinear range II, the boundary condition for the inner region at large r^* changes. For the linear range, this boundary condition for u_r at the cylinder is $(1 - z^{*2})(1 - r^{-2}) \cos \theta$. When the centrifugal term is included and Λ is increased, there are two components to the boundary condition (2.19). The first term is $2(r^* - b)(1 - z^{*2}) \cos \theta$, which is to be expected, based on the linear solution, and the second term is $\Lambda' \hat{u}_1$ (where $\Lambda' = \Lambda \epsilon^{-1}$), which has three turning points and increases linearly with Λ' (see end of § 2.2 for further discussion on this boundary condition). As the first term is dependent on $\cos \theta$ and the weighting of the second term is by Λ' , it is possible these terms are of equal magnitude, with a resulting velocity profile a combination of these two terms at different azimuthal locations for the same Λ' . For increasing Λ' , the

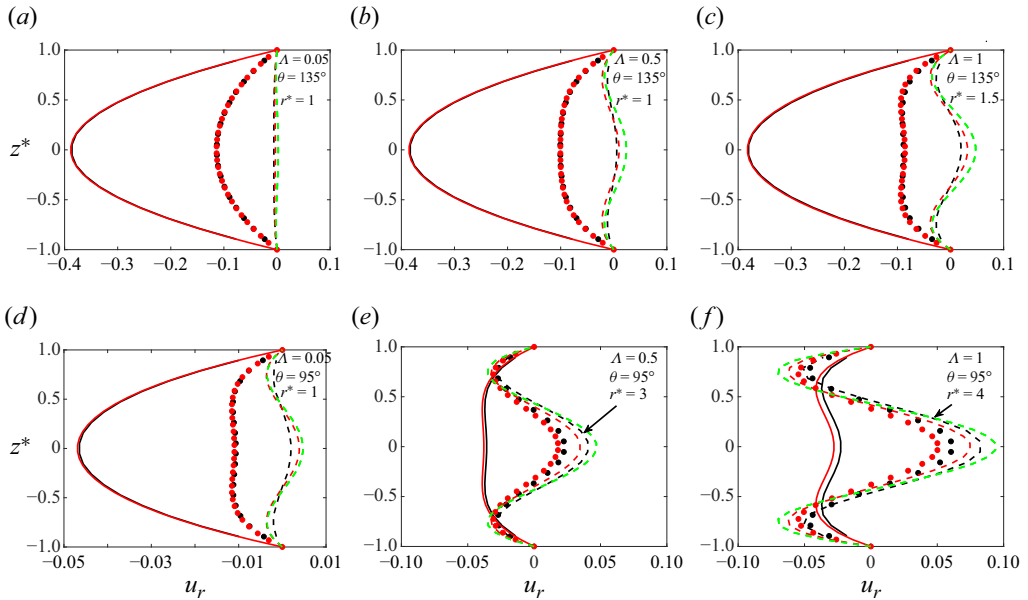


Figure 12. The radial velocity profiles (in the vertical direction) for (a–c) $\theta = 135^\circ$ and (d–f) $\theta = 95^\circ$ for $\Lambda = 0.05$ (a,d), 0.5 (b,e) and 1 (c,f). The three velocity profiles are at $r^* = 50$ (solid line), $r^* = 10$ (dots) and also the velocity profile where the numerical simulation results best match the asymptotic boundary condition (2.24) (green dashed lines). The colours represent the current numerical simulations (black) and Thompson’s outer solution (red).

three-turning-point velocity profile starts to emerge first at $\theta = \pi/2$ due to the $\sin^2 \theta$ term in \hat{u}_1 . This is the upwelling (due to the centrifugal term), which has already been discussed in the context of the generation of the counter-rotating vortices in §4.2. When Λ is still further increased into nonlinear range II, the boundary condition for u_r at large r^* only has one term, namely $\Lambda'' \hat{u}_1$.

To show the effect of varying azimuthal location and Λ , profile plots of u_r (in the vertical direction) at different radial locations from the cylinder surface are shown in figure 12, where the first row (a–c) and second row (d–f) are for $\theta = 135^\circ$ and $\theta = 95^\circ$, respectively; the latter is chosen to highlight the increased effect of inertia close to $\theta = \pi/2$. The radial locations $r^* = 50$ and $r^* = 10$ are chosen to show how the velocity profile develops from large to small r^* (note that for $\epsilon = 0.01$, $r^* = 50$ is equivalent to $0.5R$). A third velocity profile is also shown (with a dashed line), where the u_r velocity profile is taken at the radial distance that best matches the asymptotic boundary condition (2.24). This always occurred at r^* where the maximum positive u_r value was attained (see figure 6a).

Figure 12(a–c) shows that, for $\theta = 135^\circ$ and an increase in Λ , the velocity profile remains almost unchanged for $r^* = 50$, with a mild distortion arising in the profiles at $z^* = 0$ (away from a parabolic shape) at $r^* = 10$ and only resulting in the three-turning-point profile at $\Lambda = 1$. For $\theta = 95^\circ$ and $\Lambda = 0.05$, the profiles for $r^* = 1$ and $r^* = 10$ are already distorted, however; even the closest matching velocity profile is quite different from the asymptotic boundary condition. It is quite likely that, for the flow conditions at this location, the two terms mentioned above are of approximately equal magnitude.

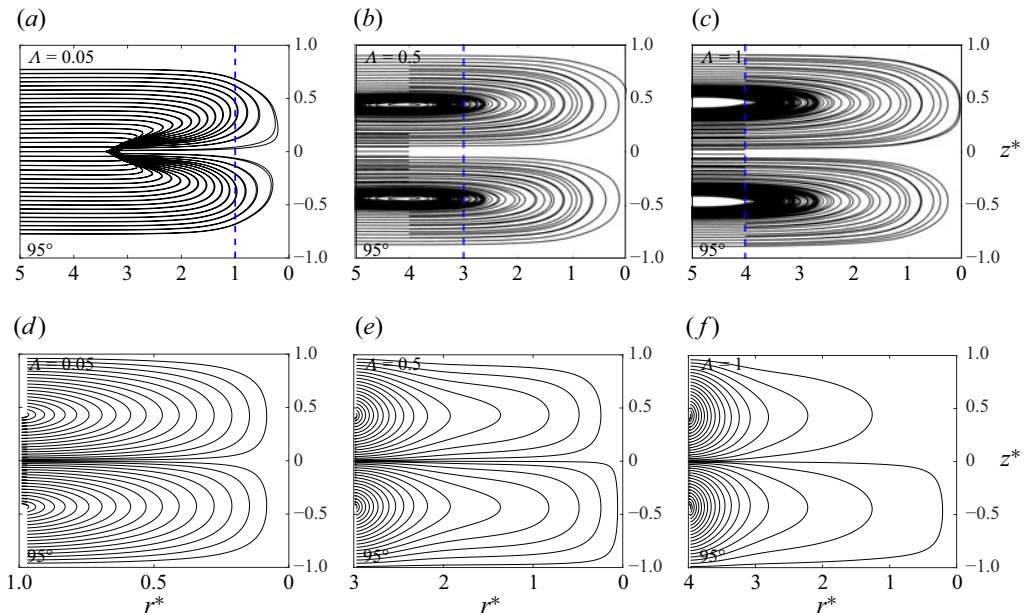


Figure 13. Streamlines of u_z and u_r in planes normal to the cylinder surface (z^*-r^*) at 98° for $\Lambda = 0.05$ (a,d), 0.5 (b,e) and 1 (c,f) for the direct numerical simulations (a–c) and nonlinear range II (2.23) (d–f). In (a–c) the blue dashed line indicates r_D^* , where the asymptotic boundary condition (2.24) best matches the current simulation results.

The reason for this in-depth look at u_r and its connection to the asymptotic boundary condition is because the nonlinear range II system of (2.23) does not have a defined domain length/size in r^* (see boundary conditions (2.24)). One possibility is to set the domain length, r_D^* , to that where the current numerical simulation data best match the asymptotic boundary condition (2.24), the length of which was found to increase as Λ increased (see figure 12d–f). Streamline plots of u_z and u_r at 98° are shown in figure 13(a–c) for the direct numerical simulations. The radial locations of r_D^* are highlighted by the blue dashed line (note that these are the dashed line velocity profiles in figure 12d–f). In figure 13(d–f) are shown the streamlines for nonlinear range II. There are considerable differences between the simulation results and the nonlinear range II streamlines, which is likely to be due to the zero vertical velocity imposed at the ‘inlet’ of nonlinear II calculations, which is not the case for the direct numerical simulations. For these confined flows, the flow field will be very sensitive to these imposed boundary conditions.

As Λ is increased, the pair of counter-rotating vortices form closer to the front stagnation point and also become larger, which results in the momentum in the radial and vertical directions increasing and hence the momentum in the azimuthal direction decreasing. The consequence is a negative displacement thickness at the front of the cylinder, which can be seen in figure 14(a–c), where the tangential velocity at $\theta = 3\pi/4$ is less than that of the potential flow as Λ is increased from 0.1 to 3. An increase in Λ also results in the adverse pressure gradient emerging at the back of the cylinder, which results in a deceleration of the tangential velocity, an effect that is quite pronounced for $\Lambda = 10$ (see figure 14f).

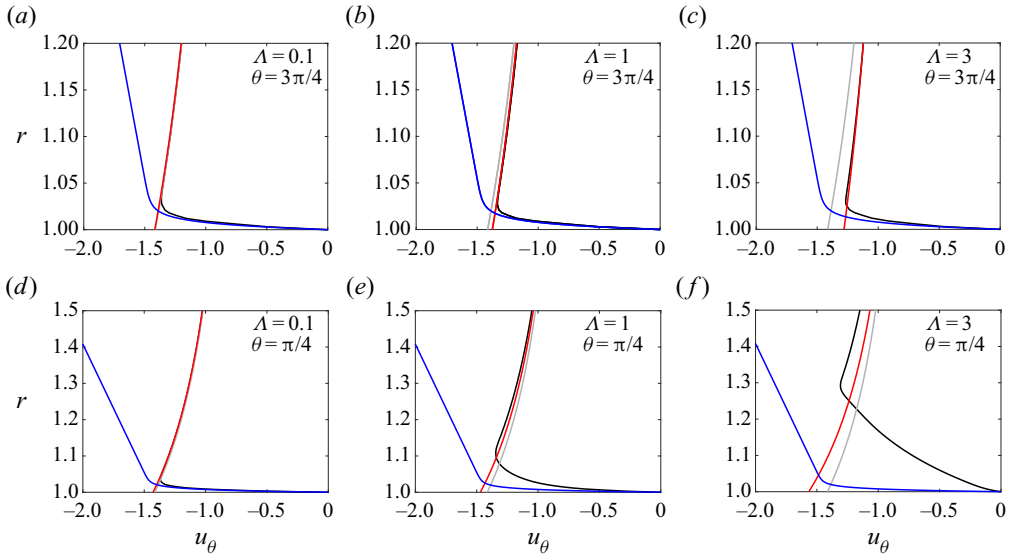


Figure 14. The tangential velocity profiles for (a–c) $\theta = 3\pi/4$ and (d–f) $\theta = \pi/4$ for $\Lambda = 0.1$ (a,d), 1 (b,d) and 3 (c,f). All profiles are in the midplane, $z = 0$. The lines represent the current Navier–Stokes numerical simulations (black line), Thompson’s inner solution (blue line), Thompson’s outer solution (red line) and the potential flow solution (grey line).

4.6. Limit of steady flow with increasing Λ

For $\Lambda \gg 1$, the channel Reynolds number $Re_h = U_c h/\nu$ becomes a potentially limiting factor to a steady flow and is especially important for flows past circular cylinders, as the fluid has to accelerate around the sides. The critical Reynolds number for flow in a channel is approximately 800 (Tuckerman *et al.* 2014), which for $\epsilon = 0.01$ is $\Lambda = 8$. The highest value for Λ that was simulated with the steady-state solver was $\Lambda = 3$ and a simulation of $\Lambda = 5$ did not converge. No further attempt was made to obtain an exact point of transition with a transient solver or to investigate the instability mechanism. How this upper limit on Re_h affects the flow past a circular cylinder is discussed further in § 6.

4.7. Drag force

The force on the cylinder is

$$\mathbf{F} = \int_S (\tilde{p}\mathbf{l} - \boldsymbol{\tau}) \cdot \hat{\mathbf{n}} \, dS, \tag{4.1}$$

where \mathbf{l} and $\boldsymbol{\tau}$ are the identity matrix and viscous stress tensor, respectively, and $\hat{\mathbf{n}}$ is the unit vector out of the fluid domain. The corresponding drag coefficient is defined as

$$C_D = \frac{\mathbf{F} \cdot \hat{\mathbf{x}}}{2\rho U_c^2 hR}, \tag{4.2}$$

which can be split into the pressure and the viscous components,

$$C_{DP} = \frac{\int_S \tilde{p}\hat{\mathbf{n}} \cdot \hat{\mathbf{x}} \, dS}{2\rho U_c^2 hR}, \quad C_{Dv} = C_D - C_{DP}, \tag{4.3a,b}$$

where $\hat{\mathbf{x}}$ is the unit vector in the streamwise direction (Klettner *et al.* 2016). The drag coefficient is plotted in figure 15(b) with the numerical simulations compared with Lee &

Flow past a cylinder in a Hele-Shaw configuration

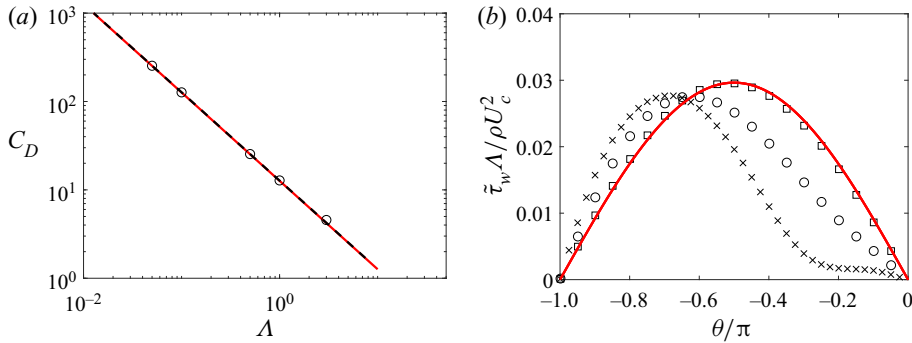


Figure 15. (a) Drag coefficient as a function of Λ ; the current numerical simulations are shown as circles, Lee & Fung's (1969) force expression for a Stokes flow past a cylinder is shown as a black dashed line and Thompson's analytical solution is given by the red lines. All results are for $\epsilon = 0.01$. (b) The midplane friction coefficient for $\Lambda = 0.1$ (\square), 1 (\circ) and 3 (\times).

Fung's (1969) Stokes solution and also a direct calculation with (4.1) using Thompson's analysis. The two methods give the same prediction, although Thompson's analysis gives a better agreement for the surface pressure for $\Lambda = 3$ (figure 8c), which is due to the form of the Λ term in (B4).

An alternative way of calculating the drag force would be using an integral analysis, where, due to diffusion, velocity perturbations in the wake disappear quickly behind the cylinder (Lee & Fung 1969). The friction coefficient $\tilde{\tau}_w \Lambda / (\rho U_c^2)$ with $\tilde{\tau}_w = \mu \partial \tilde{u}_\theta / \partial \tilde{r}$ on the cylinder midplane is plotted for the direct numerical simulations and Thompson's (1968) inner solution in figure 15(b) for increasing Λ . The boundary layer thickness around the front of the cylinder decreases slightly for increasing Λ , leading to an increase in the shear stress for $-1 < \theta/\pi < -1/2$ (figure 15b), which is not predicted by Thompson's inner solution, as it has no dependence on Λ (see (B3)). Agreement is good up to where the inner solution is applicable; however, the deceleration of the tangential velocity is not captured at the rear of the cylinder. The friction coefficient is two orders of magnitude less than the pressure and also decreases significantly towards the sidewalls, which results in $C_{DP}/C_D \approx 1$.

5. Results: variation of ϵ

In this section the variation of ϵ is investigated with $\epsilon = 0.1$ and varying Λ . The main difference in increasing Λ at $\epsilon = 0.1$ is that the channel instability occurs now at $\Lambda = 80$, which means that the flow features already analysed in § 4 can develop further, and also results in additional flow phenomena. Also, simulations are carried out to explore the parameter space Λ - ϵ , and these results are discussed in the next section.

The metric θ_v was found to be quite different for $\epsilon = 0.1$ than for $\epsilon = 0.01$. Figure 16(a) shows that the angle at which the secondary flow starts to form is closer to $\theta/\pi = 1/2$ and also that θ_v is quite insensitive to Λ for $\Lambda \gg 1$. For $\epsilon = 0.1$, the boundary layer is thicker than for $\epsilon = 0.01$, which results in the tangential velocity having a smaller magnitude around the front of the cylinder (compare figure 14(d-f) with figure 17), which means that the centrifugal effect that causes the secondary flow is weakened, and as such the vortices form further away from the front stagnation point. Figure 16(b) shows the variation of the metric L_v with Λ (at $\theta = 98^\circ$). For $\Lambda = 1$ the counter-rotating vortices are quite similar in

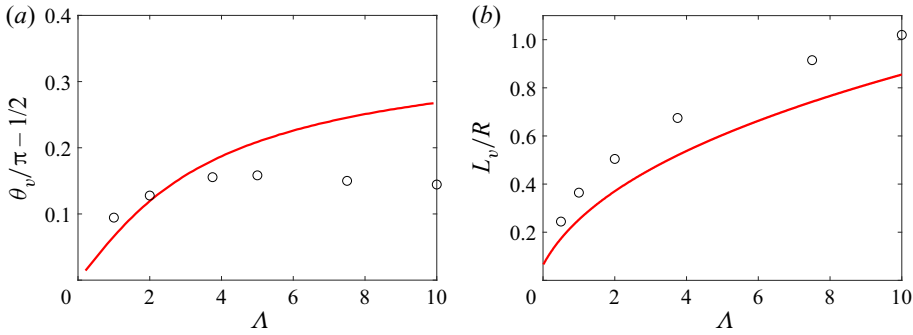


Figure 16. (a) Variation of the angle θ_v with Λ . (b) Variation of the size of the counter-rotating vortices with Λ in the midplane at 98° . Thompson's analytical solution is given by the red line. All results are for $\epsilon = 0.1$.

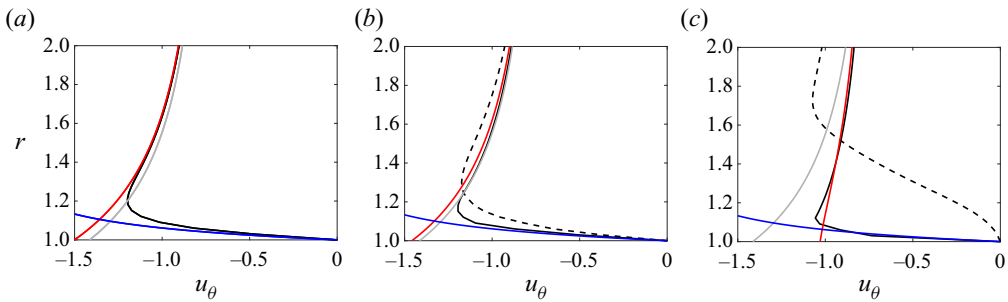


Figure 17. The tangential velocity profiles for $\epsilon = 0.1$ and $\Lambda = 0.1$ (a), 1 (b) and 10 (c) at $\theta = 3\pi/4$. All profiles are in the midplane. The lines represent the current numerical simulations (black line), Thompson's inner solution (blue line), Thompson's outer solution (red line) and the potential flow solution (grey line). To highlight the deceleration at the back of the cylinder, the dashed line in panels (b) and (c) is the velocity profile at $\theta = \pi/4$.

size to $\epsilon = 0.01$ (both are $L_v/R \approx 0.2$; see figure 7b). For $\Lambda = 10$, these grow to $L_v/R \approx 1$. The prediction from Thompson's analysis is also shown; however, it should be noted that this is taken well past where it is applicable. Additional simulations were also carried out to investigate the effect of increasing ϵ on the secondary flow. As ϵ was increased from 0.2 to 0.5, the secondary flow that is generated is smaller and confined closer to the sidewalls as compared to $\epsilon = 0.01$ (see for example figure 5).

The tangential velocity profiles follow those seen previously for ϵ , with good agreement between the direct numerical simulations and Thompson's solution (see figure 17). The displacement thickness is clearly visible in figure 17(a), as the red line is 0.6ϵ above the potential flow solution. Although there is no negative displacement thickness at $\Lambda = 1$, the tangential velocity for $\Lambda = 10$ is considerably less than the potential flow solution. The comparison is good at the front of the cylinder, even for $\Lambda = 10$. To highlight the effect of the adverse pressure gradient at the back of the cylinder, a profile is also given at $\pi/4$ with significant deceleration for $\Lambda = 10$.

For $\epsilon = 0.1$, the midplane friction and the surface pressure coefficient are plotted in figure 18. Similar to $\epsilon = 0.01$, there is good agreement for the surface pressure coefficient for $\Lambda = 0.1$ and 1. For $\Lambda = 10$ there is an adverse pressure gradient at $\theta/\pi \approx \pm 0.4$. Owing to the deceleration in the tangential velocity at the rear of the cylinder, the friction coefficient is negligible here for $\Lambda = 10$. Note the increase in the friction coefficient

Flow past a cylinder in a Hele-Shaw configuration

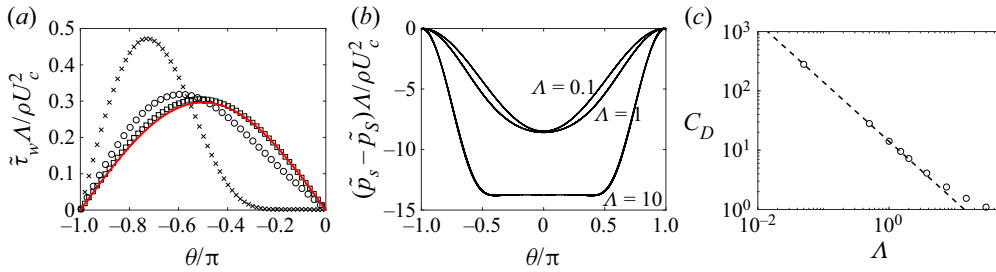


Figure 18. (a) The midplane friction coefficient for $\Lambda = 0.1$ (\square), 1 (\circ) and 10 (\times). (b) The pressure coefficient for $\Lambda = 0.1$, 1 and 10 . (c) Drag coefficient as a function of Λ ; the current numerical simulations are shown as circles, Lee & Fung's (1969) force expression for a Stokes flow past a cylinder is shown as a black dashed line and Thompson's analytical solution is given by the red line. All results are for $\epsilon = 0.1$.

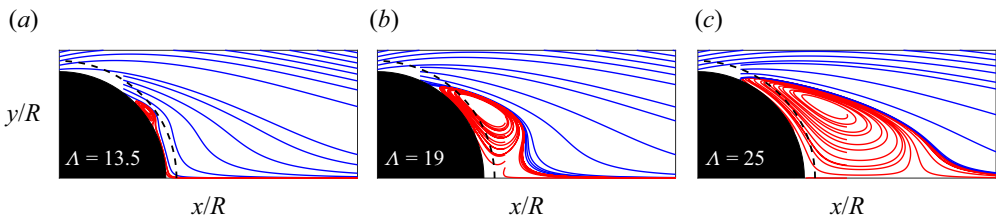


Figure 19. Streamlines of the velocity field (in blue) highlighting the development of the laminar separation bubble (red streamlines) in the midplane for $\epsilon = 0.1$ and $\Lambda = 13.5$ (a) ($\approx \Lambda_s$), 19 (b) and 25 (c). The black dashed line indicates the distance ϵ from the cylinder surface. The flow is from left to right.

over the front side of the cylinder for $\Lambda = 10$. In comparison to $\epsilon = 0.01$, the friction coefficient is only an order of magnitude less than the pressure coefficient, which results in the pressure component of the drag coefficient being $C_{DP}/C_D \approx 0.95$. The dependence of C_D on ϵ (see Lee & Fung 1969) is present, but it is not possible to distinguish this from figures 15 and 18.

The consequence of the adverse pressure gradient and the subsequent deceleration in the tangential velocity is a laminar separation bubble (LSB) forming at the rear of the cylinder for $\Lambda_s \approx 13.5$ (Λ_s here is the minimum value of Λ at which the LSB forms). Figure 19 shows streamlines of the velocity field in blue while the LSB is highlighted with red streamlines. The LSB is of size $O(h)$ as indicated by the black dashed line around the cylinder. When Λ is further increased, the LSB forms into an attached separation bubble, which is seen in two-dimensional flow past cylinders up to a Reynolds number of about 40. Figure 20 shows that decreasing ϵ decreased the size of the LSB and also shifted its formation towards the front stagnation point. Also, as ϵ decreases, Λ_s increases.

6. Discussion and conclusions

Our concern in the paper has been with the effects of increasing nonlinearity, represented by increasing values of the parameter Λ , in a Hele-Shaw configuration with a circular cylinder in a channel. The study has consisted of direct numerical simulations for small finite ratios (ϵ) of channel half-height to cylinder radius supplemented by analyses for asymptotically small ratios.

It is insightful to summarise the work in the preceding sections into a plot of the parameter space $\Lambda-\epsilon$ (see figure 21). Traditional Hele-Shaw flow is for $\Lambda \ll 1$ and $\epsilon \ll 1$.

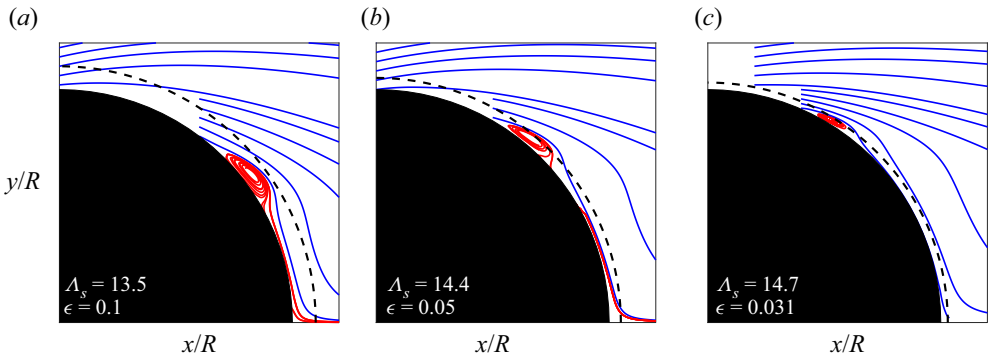


Figure 20. Streamlines of the velocity field (in blue) highlighting the laminar separation bubble (red streamlines) in the midplane ($z = 0$) for $\epsilon = 0.1$ (a), 0.05 (b) and 0.031 (c) for $\Lambda \approx \Lambda_s$. The black dashed line indicates the half-height h . The flow is from left to right.

In § 2 the linear range and the nonlinear ranges I, II and III were identified, which correspond to Λ being $O(\epsilon)$, $O(\epsilon^{1/2})$ and $O(1)$, respectively. In § 4 the upper limit, as Λ is increased, of the steady flow was suggested as due to unsteady Poiseuille flow (shown as a green dashed line). In § 5, as ϵ was increased to approximately $0.3 < \epsilon < 0.5$, the secondary flow was no longer present as two counter-rotating vortices; instead, smaller vortices formed adjacent to the sidewalls (represented by a red dashed line). Also there is the steady separated flow region for $\epsilon \gtrsim 0.03$ and increasing Λ . The region where Thompson's inner and outer analyses are applicable is for $\Lambda = O(\epsilon)$ and $O(1)$, respectively, and $\epsilon \ll 1$. In nonlinear range I, the secondary flow starts to emerge, and this is followed by a negative displacement thickness at the front of the cylinder in nonlinear range II and a deceleration of the tangential velocity around the back of the cylinder in nonlinear range III. The suggested form of nonlinear range III implies that the three-dimensional interactive boundary layer (IBL) equations hold throughout the outer region then. Three-dimensional IBL theory is usually used for external flows (Smith 1983; Duck & Burggraf 1986; Smith 2018) rather than for the present internal configuration.

Further investigation is required to establish how and when the unsteady flow might occur as Λ is increased. There are two different flow fields that can be present before the unsteadiness occurs, namely a steady separated flow (for $0.2 \gtrsim \epsilon \gtrsim 0.03$) and a non-separated flow ($\epsilon \lesssim 0.03$), which are likely to respond differently to an increase in Λ . Additionally, as the flow has to accelerate around the cylinder, the flow might go unsteady earlier than indicated in the figure (i.e. the dashed green line in figure 21 could be shifted to the left). The three-dimensional nature of these separation bubbles is also left to further work.

In this work there was extensive comparison made between our reduced calculations in nonlinear range I, direct numerical simulations and Thompson's analysis. Thompson's use of matched asymptotics meant that there was some feedback between the inner and outer regions. There is interesting overlap of Thompson's and the present analytical work. Thompson's excellent work is mostly concerned with effects such as higher-order influences in the outer region. In contrast, we find analytically that nonlinearity first enters at leading order in the inner region as far as the secondary flow is concerned and, in a second stage, nonlinearity is much increased to the extent that the main flow velocity component becomes altered nonlinearly. Both of these inner-region stages occur with the parameter Λ still being small. The advantage of treating the fully nonlinear problem by

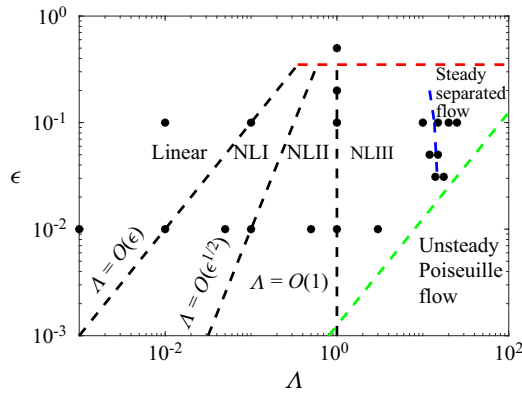


Figure 21. A diagram summarising the different ranges for the flow past a circular cylinder in a Hele-Shaw configuration with the linear and nonlinear (NL) ranges I, II and III analysed in § 2. The dashed red line indicates the approximate upper limit of the formation of the secondary flow (as two counter-rotating vortices as in figure 5) and the dashed green line indicates the approximate transition to an unsteady Poiseuille flow. The blue dashed line indicates steady separated flow. The simulations carried out are indicated by ●.

direct simulation, allied with analysis, is felt to be that clear ranges can be identified when certain phenomena are likely to occur.

Acknowledgements. The authors acknowledge the use of University College London’s Myriad High Performance Computing Facility (Myriad@UCL) and Kathleen High Performance Computing Facility (Kathleen@UCL), and associated support services, in the completion of this work.

Declaration of interests. The authors report no conflict of interest.

Author ORCIDs.

- C.A. Klettner <https://orcid.org/0000-0002-3944-4907>;
- F.T. Smith <https://orcid.org/0000-0003-4850-995X>.

Author contributions. C.A.K. performed the OpenFoam numerical simulations. F.T.S. carried out the asymptotic analysis. Both authors contributed equally to analysing data, reaching conclusions and writing the paper.

Appendix A

This appendix will detail the mesh independence study. Boundary layers in Hele-Shaw flow are not like the more common inviscid–viscous boundary layers (where the boundary layer thickness can be estimated by equating viscous and inertial forces). Here the boundary layer thickness does not vary significantly with Δ and is dependent on the gap height $2h$. As this is a three-dimensional problem, mesh independence will be shown in the three cylindrical coordinates.

Firstly, for the radial and azimuthal directions, the case of $\epsilon = 0.01$ and $\Delta = 0.001$ is chosen. From figure 4, we can see that, although the boundary layer thickness is $r^* = 2$, the gradient of the vertical velocity changes sign at $r^* \approx 0.5$, making u_z the velocity component with the highest mesh resolution requirement. Figure 22 shows meshes of increasing radial resolution $\Delta_r/R = \{0.0017, 0.0011, 0.0008\}$ or $\Delta_r/h = \{0.17, 0.11, 0.08\}$, with the coarsest visibly not resolving the vertical velocity close to the wall while the finest mesh adequately resolves it.

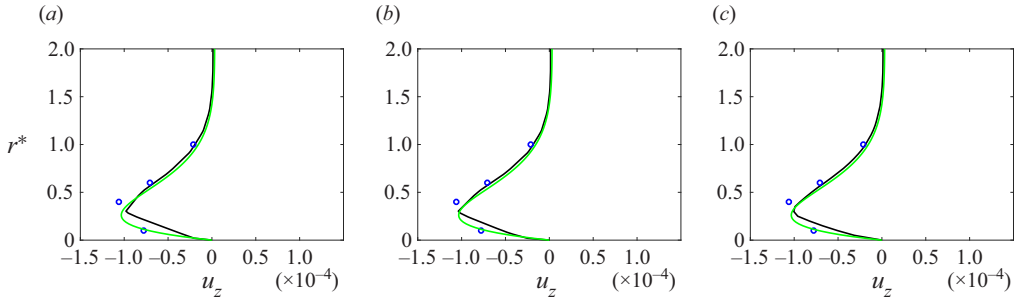


Figure 22. Mesh independence study of the vertical velocity at $\theta = 3\pi/4$ for $\epsilon = 0.01$, $\Lambda = 0.001$ and $z^* = 0.4$ for $\Delta_r/h = 0.17$ (a), 0.11 (b) and 0.08 (c). The vertical mesh resolution is shown to the left of the velocity profiles. Also shown are the current reduced simulations for nonlinear range I (green lines) and Thompson’s inner solution (blue circles).

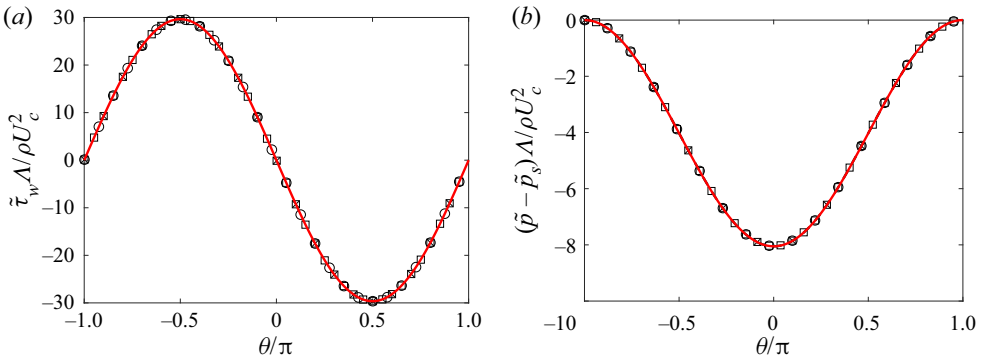


Figure 23. Mesh independence study of (a) the friction coefficient and (b) the pressure coefficient for $\epsilon = 0.01$, $\Lambda = 0.001$ and $z^* = 0$ with $\Delta_r/h = 0.17$ (\square), 0.11 (\circ) and 0.08 (\times). Also shown are Thompson’s inner solution for the friction coefficient and the outer solution for the pressure (red lines).

It should be noted that the mesh resolution required for the vertical velocity is considerably greater than the tangential velocity. To highlight this, the friction coefficient $\tilde{\tau}_w \Lambda / (\rho U_c^2)$ on the cylinder midplane is plotted and compared to Thompson’s analytical solution, with all resolutions showing excellent agreement (see figure 23). Additionally, the pressure coefficient is shown, which highlights that these surface metrics are not sensitive to the meshes used. Additional integral metrics (e.g. drag coefficient) have not been included in this mesh independence study, as the surface metrics indicate that an adequate resolution is present. This also indicates that the resolution requirement in the azimuthal direction is not as great in the radial direction, and so $\Delta_\theta \approx 4\Delta_r$.

For the vertical direction, the case chosen for mesh independence is $\Lambda = 1$ and $\epsilon = 0.01$. The vertical profile of the radial velocity u_r (i.e. in the z^* -direction) at $r^* = 4$ was chosen (see figure 12f), as the velocity profile has three turning points, therefore requiring a higher resolution than the parabolic profiles usually encountered in Hele-Shaw type flows. Radial velocity profiles were compared for increasing mesh densities of $\Delta_z/h = \{0.095, 0.065, 0.049\}$ (while keeping $\Delta_r/h = 0.08$) and all meshes provided adequate resolution (plots not shown here).

The final meshes used a mesh resolution close to the cylinder of $\Delta_r/h = 0.08$, $\Delta_\theta = 0.32$ and $\Delta_z = 0.049$. In the vertical direction, the mesh spacing is equal whereas the

mesh spacing in the radial direction is finer towards the cylinder surface. Note that away from the cylinder the mesh size increases, which results in quite elongated elements far from the cylinder. However, the Poiseuille flow that is present in this region is insensitive to these elements.

Appendix B

This appendix states Thompson’s (1968) tangential and radial velocities and pressure for the outer and inner flow regions. The outer solution for the tangential velocity is given by

$$\begin{aligned}
 u_\theta = & \underbrace{-(1 - z^{*2}) \left(1 + \frac{1}{r^2}\right) \sin \theta}_{O(1)} - \underbrace{\frac{1}{2} \epsilon (1 - z^{*2}) \frac{\phi_1 \sin \theta}{r^2}}_{O(\epsilon)} \\
 & - \underbrace{\frac{1}{18} \epsilon^2 \phi_1^2 (1 - z^{*2}) \frac{\sin \theta}{r^2} + \Lambda H(z^*) \frac{\sin 2\theta}{r^3}}_{O(\epsilon^2)}, \tag{B1}
 \end{aligned}$$

where $H(z^*) = z^{*6}/15 - z^{*4}/3 + 11z^{*2}/35 - 1/21$ and $\phi_1 = 2.521$; and the radial velocity is given by

$$\begin{aligned}
 u_r = & \underbrace{(1 - z^{*2}) \left(1 - \frac{1}{r^2}\right) \cos \theta}_{O(1)} - \underbrace{\frac{1}{2} \epsilon (1 - z^{*2}) \frac{\phi_1 \cos \theta}{r^2}}_{O(\epsilon)} \\
 & - \underbrace{\frac{1}{18} \epsilon^2 \phi_1^2 (1 - z^{*2}) \frac{\cos \theta}{r^2} + \Lambda H(z^*) \left(\frac{\cos 2\theta}{r^3} - \frac{1}{r^5}\right)}_{O(\epsilon^2)}. \tag{B2}
 \end{aligned}$$

The inner solution for the tangential velocity, to $O(\epsilon)$, is given by

$$\begin{aligned}
 u_\theta = & \underbrace{-2 \left(1 - z^{*2} - 4 \sum_{n=0}^{\infty} (-)^n k_n^{-3} e^{-k_n r^*} \cos k_n z^*\right) \sin \theta}_{O(1)} \\
 & - \frac{1}{2} \epsilon \sin \theta \underbrace{\left\{ \left((1 - z^{*2})(\phi_1 - 4r^*) - \phi_1 \sum_{n=0}^{\infty} (-)^n k_n^{-3} e^{-k_n r^*} \cos k_n z^* \right) \right\}}_{O(\epsilon)}, \tag{B3}
 \end{aligned}$$

where $k_n = (n + 1/2)\pi$. The inner solutions, to $O(\epsilon)$, for the radial and vertical velocities are tabulated in Thompson (1968). The outer pressure, to $O(\epsilon^2)$, in Thompson (1968) is given by

$$p = -2 \cos \theta \left(r + \frac{1 + \frac{1}{2} \epsilon \phi_1 + \frac{1}{18} \epsilon^2 \phi_1^2}{r} \right) - \frac{12}{35} \Lambda \left(1 - \frac{2 \cos 2\theta}{r^2} + \frac{1}{r^4} \right), \tag{B4}$$

noting the typographical error in Thompson’s (1968) equation (4.12).

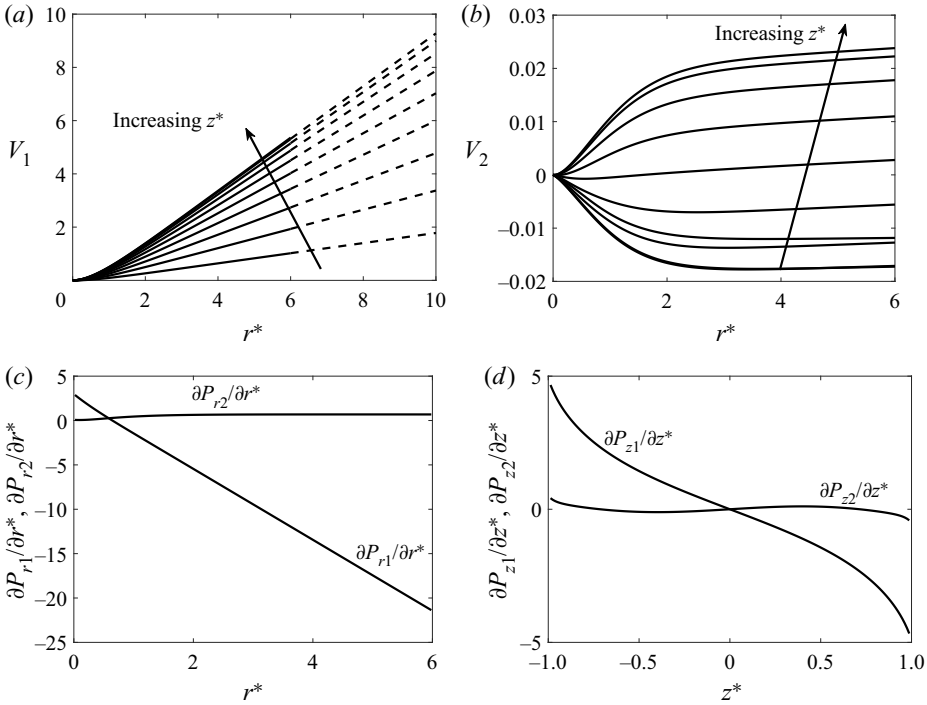


Figure 24. The variation of the functions (a) V_1 , (b) V_2 and (c) $\partial P_{r1}/\partial r^*$ and $\partial P_{r2}/\partial r^*$ with radial distance, and (d) $\partial P_{z1}/\partial z^*$ and $\partial P_{z2}/\partial z^*$ with vertical position. Panels (a) and (b) show different values of z^* from -0.9 to 0 , (c) are the midplane values and (d) are for the cylinder surface. The dashed lines in (a) are the functions $V_{1\infty}$.

Appendix C

In this appendix the solution to nonlinear range I, (2.13) and (2.16), is described. The radial velocity u_r close to the cylinder is given by

$$u_r = 2V_1(r^*, z^*)\epsilon \cos \theta + 4V_2(r^*, z^*)\Lambda \sin^2 \theta, \quad (C1)$$

while further out the above expression reduces to

$$u_r = 2V_{1\infty}(r^*, z^*)\epsilon \cos \theta + 4V_{2\infty}(z^*)\Lambda \sin^2 \theta, \quad (C2)$$

with

$$V_{1\infty}(r^*, z^*) = (r^* - b)(1 - z^{*2}), \quad V_{2\infty}(z^*) = \frac{1}{42} - \frac{11}{70}z^{*2} + \frac{1}{6}z^{*4} - \frac{1}{30}z^{*6}, \quad (C3a,b)$$

where $b = 0.63$. The functions V_1 , V_2 and $V_{1\infty}$ are plotted in figure 24(a,b). The gradient of the pressure perturbation in the radial and vertical directions in nonlinear range I are given by

$$\frac{\partial \hat{p}}{\partial r^*} = 2 \frac{\partial P_{r1}}{\partial r^*} \cos \theta + \frac{\partial P_{r2}}{\partial r^*} \left(\frac{4\Lambda}{\epsilon} \right) \sin^2 \theta \quad (C4)$$

and

$$\frac{\partial \hat{p}}{\partial z^*} = 2 \frac{\partial P_{z1}}{\partial z^*} \cos \theta + \frac{\partial P_{z2}}{\partial z^*} \left(\frac{4\Lambda}{\epsilon} \right) \sin^2 \theta, \quad (C5)$$

respectively, where the additional functions on the right-hand sides are plotted in figure 24(c,d).

REFERENCES

- BALSA, T.F. 1998 Secondary flow in a Hele-Shaw cell. *J. Fluid Mech.* **372**, 25–44.
- BATCHELOR, G.K. 1967 *An Introduction to Fluid Dynamics*, 1st edn. Cambridge University Press.
- BUCKMASTER, J. 1970 Some remarks on Hele-Shaw flow and viscous tails. *J. Fluid Mech.* **41**, 523–530.
- DUCK, P.W. & BURGGRAF, O.R. 1986 Spectral solutions for three-dimensional triple-deck flow over surface topography. *J. Fluid Mech.* **162**, 1–22.
- FU, T. 2016 Microfluidics in CO₂ capture sequestration and applications. In *Advances in Microfluidics - New Applications in Biology, Energy and Materials Sciences* (ed. X.-Y. Yu), pp. 293–313. InTech, London.
- GLOWINSKI, R. & PIRONNEAU, O. 1979 Numerical methods for the first biharmonic equation and for the two dimensional Stokes problem. *SIAM Rev.* **21**, 167–212.
- GUGLIELMINI, L., RUSCONI, R., LECUYER, S. & STONE, H.A. 2011 Three-dimensional features in low-Reynolds-number confined corner flows. *J. Fluid Mech.* **668**, 33–57.
- HELE-SHAW, H.S. 1898 The flow of water. *Nature* **58**, 34–36.
- HELE-SHAW, H.S. 1899 Streamline motion of a viscous film. In *Rept. 68th Mtg. British Assoc. Advanc. Sci.*, pp. 136–142. John Murray.
- KIMURA, H., SAKAI, Y. & FUJII, T. 2018 Organ/body-on-a-chip based on microfluidic technology for drug discovery. *Drug Metab. Pharmacokinet.* **33**, 43–48.
- KLETTNER, C.A., EAMES, I., SEMSARZADEH, S. & NICOLLE, A. 2016 The effect of a uniform through-surface flow on a cylinder and sphere. *J. Fluid Mech.* **793**, 798–839.
- LEE, J.S. 1969 Slow viscous flow in a lung alveoli model. *J. Biomech.* **2**, 187–198.
- LEE, J.S. & FUNG, Y.C. 1969 Stokes flow around a circular cylindrical post confined between two parallel plates. *J. Fluid Mech.* **37**, 657–670.
- NIVEDITA, N., LIGRANI, P. & PAPAUTSKY, I. 2017 Dean flow dynamics in low-aspect ratio spiral microchannels. *Sci. Rep.* **7**, 44072.
- RIBEIRO, V.M., COELHO, P.M., PINHO, F.T. & ALVES, M.A. 2012 Three-dimensional effects in laminar flow past a confined cylinder. *Chem. Engng Sci.* **84**, 155–169.
- RIEGELS, F. 1938 Zur kritik des Hele-Shaw-Versuchs. *Z. Angew. Math. Mech.* **18**, 95–106.
- SMITH, F.T. 1983 Properties, and a finite-difference approach, for interactive three-dimensional boundary layers. *UTRC Rep. UT 83-46*, East Hartford, Conn. (See also *Annu. Rev. Fluid Mech.* 1986).
- SMITH, F.T. 2018 Shear flow over flexible three-dimensional patches in a surface. *Phil. Trans. R. Soc. A* **376**, 20170348.
- SMITH, F.T. & DENNIS, S.C.R. 1990 Computations on flow past an inclined flat plate of finite length. *J. Engng Maths* **24**, 311–321.
- SZNITMAN, J., GUGLIELMINI, L., CLIFTON, D., SCOBEE, D., STONE, H.A. & SMITS, A.J. 2012 Experimental characterization of three-dimensional corner flows at low Reynolds numbers. *J. Fluid Mech.* **707**, 37–52.
- THOMPSON, B.W. 1968 Secondary flow in a Hele-Shaw cell. *J. Fluid Mech.* **31**, 379–395.
- TSAY, R.Y. & WEINBAUM, S. 1991 Viscous flow in a channel with periodic cross-bridging fibres: exact solutions and Brinkman approximation. *J. Fluid Mech.* **226**, 125–148.
- TUCKERMAN, L.S., KREILOS, T., SCHROBSDORFF, H., SCHNEIDER, T.M. & GIBSON, J.F. 2014 Turbulent-laminar patterns in plane Poiseuille flow. *Phys. Fluids* **26**, 114103.
- WELLER, H.G., TABOR, G., JASAK, H. & FUREBY, C. 1998 A tensorial approach to computational continuum mechanics using object-oriented techniques. *Comput. Phys.* **12**, 620–631.
- ZHAK, V.D., NAKORYAKOV, V.E. & SAFONOV, S.A. 1986 Flow about a cylinder in a narrow gap at high velocities. *J. Fluid Mech.* **774**, 37–66.
- ZIMMERMAN, R.W. & BODVARSSON, G.S. 1996 Hydraulic conductivity of rock fractures. *Trans. Porous Med.* **12**, 1–30.
- ZOUACHE, M.A., EAMES, I. & LUTHERT, P.J. 2015 Blood flow in the choriocapillaris. *J. Fluid Mech.* **774**, 37–66.
- ZOUACHE, M.A., EAMES, I., KLETTNER, C.A. & LUTHERT, P.J. 2016 Form, shape and function: segmented blood flow in the choriocapillaris. *Sci. Rep.* **6**, 35754.